



## MASTER'S THESIS

CAPTAIN JOEL C. MILLER, UNITED STATES AIR FORCE

GEORGIA INSTITUTE OF TECHNOLOGY

IN PARTIAL FULFILMENT OF THE REQUIREMENTS FOR THE AWARD OF  
MASTER OF SCIENCE IN MECHANICAL ENGINEERING

### ABSTRACT

The goal of this research is to modulate the dynamic stiffness profile of a brushless linear DC motor. There is a great deal of research demonstrating the critical role the dynamic stiffness of a machine tool plays in machining processes. Depending on the operation performed and the material of the machined part, different profiles of dynamic stiffness result in varying work piece surface finish, stability margins and process efficiency. Currently, the dynamic stiffness of a machine tool has been strictly dependent on its physical composition. Consequently, the machining process is designed around a machine tool's existing dynamic stiffness. The ability to change the dynamic stiffness of linear drives employed as main feed mechanisms will provide tremendous flexibility to machine tools by allowing the dynamic stiffness to be designed around the desired process.

This research includes performing comprehensive system identification of the controller, amplifier and motor system, developing analytical results varying controller parameters to change resonant frequencies and amplitudes of the stiffness profile. Experimental data are obtained for comparison to predicted results. The resultant stiffness of the controlled system is analyzed to determine the relative success of the control system. In addition, several alternative controller designs are developed and analytically studied for possible future implementation.

MODULATING DYNAMIC STIFFNESS OF A DIRECT-DRIVE BRUSHLESS  
LINEAR DC MOTOR

A Thesis  
Presented to  
The Academic Faculty

by


Joel Christopher Miller, Captain, USAF


In Partial Fulfillment  
of the Requirements for the Degree  
Master of Science in Mechanical Engineering

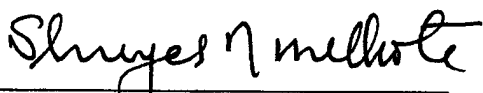
Georgia Institute of Technology  
June 1998

MODULATING DYNAMIC STIFFNESS OF A DIRECT-DRIVE BRUSHLESS  
LINEAR DC MOTOR

Approved:

  
Thomas R. Kurfess, Ph.D., Chair

  
Steven Y. Liang, Ph.D.

  
Shreyes N. Melkote, Ph.D.

Date Approved: 18 May 1998

## DEDICATION

I dedicate the completion of this thesis to my loving wife, Anita, and our precious daughter, Faith Anne. Their steadfast love and support provided boundless motivation to work through the difficulties presented by this research.

## ACKNOWLEDGMENTS

This research was supported by the Air Force Institute of Technology under sponsorship from the United States Air Force Academy Department of Astronautics. I am grateful for their confidence in me and sponsorship for this prestigious program.

This work was partially funded by the National Science Foundation under Grant Number DDM-9350159. The government has certain rights in this material. Any opinions, findings and conclusions or recommendations are those of the author and do not necessarily reflect the views of the National Science Foundation.

## TABLE OF CONTENTS

DEDICATION	iii
ACKNOWLEDGMENTS	iv
LIST OF TABLES	viii
LIST OF FIGURES	ix
NOMENCLATURE	xii
SUMMARY	xiii
I. INTRODUCTION	1
Problem Statement	2
System Identification	3
Model Verification	3
Use of Existing Control Structure to Modify Stiffness Profile	3
Develop Several Control Schemes for Future Use and Perform Theoretical Analysis	3
II. LITERATURE REVIEW/BACKGROUND	4
Brushless Linear DC Motors	4
Motor Theory	5
Commutation	8
Modeling Brushless DC Motors	11
Linear Motor Description	11
Advantages of Linear Motors in Machining	13
Linear Motor Disadvantages	14
Uses in Machining Applications	15

Dynamic Stiffness	16
Concept of Dynamic Stiffness	16
Dynamic Stiffness Implications on Machining Performance	18
Stability	18
Other Measures of Machining Performance	22
System Identification	24
Control Strategies	26
Dynamic Compliance Control as Disturbance Rejection	26
LQG/LTR Control	31
Parameter Optimization	38
Method of Inequalities	39
Edmund's Algorithm	40
Related Research	42
Chapter Conclusion	42
III. INSTRUMENTATION AND EQUIPMENT	43
Equipment Description	43
Dynamic Stiffness Measurement	44
IV. PROCEDURES	47
System Identification	47
Controller	49
System Plant	50
Transfer Function Validation	59
Control Strategy	62
Choosing Controller Gains to Change Natural Frequency and Damping Ratio	63
Force Feedforward Controller	68



LQG/LTR	70
Placing Existing Controller Poles as Close as Possible to LQG/LTR Controller	74
Conversion to Discrete-Time System for Digital Control	74
Chapter Conclusion	75
V. RESULTS FOR DYNAMIC STIFFNESS MODULATION	76
Changing Control Gains of Fixed Controller	76
Shifting Resonant Frequency and Damping Ratio	78
Analytical Results for LQG/LTR	81
Force Feedforward Control	83
VI. DISCUSSION/CONCLUSIONS	85
Challenges for Modulating Dynamic Stiffness	85
Assessment of Model Performance	85
Predicting Damping Ratios and Resonant Frequencies	86
Limitations of Fixed-Structure Controller	87
Assessing the Usefulness of Alternate Control Approaches	89
Conclusion	90
VII. RECOMMENDATIONS FOR FUTURE WORK	92
Use a Linear Motor in a Machining Process to Assess Its Relative Merits	92
Open-Architecture Controller	92
Develop Tracking Control Concurrently to Optimize Tradeoff with Compliance	
Control	93
Model Brushless Motor Phases	93
REFERENCES	94

## LIST OF TABLES

Table	Page
Table 2-1. Relative Merits of Linear Motion Devices	14
Table 4-1. System Parameter Values.	49
Table 4-2. Controller Gain Ranges for Validity of 2nd-Order Approximation.	68
Table 5-1. Control Gains Used for Target Resonant Frequencies.	80

## LIST OF FIGURES

Figure	Page
Figure 2-1. Motor Electrical Circuit for Permanent Magnet Motor.	5
Figure 2-2. Back EMF Wave Form of a Motor Coil.	7
Figure 2-3. Configuration of Three Phase Coil Phased $120^\circ$ Apart.	8
Figure 2-4. Back EMF Wave Form for Three-Phase Winding.	8
Figure 2-5. 3-Step Commutation Points for a 3-Phase Motor.	9
Figure 2-6. 6-Step Commutation Points for a 3-Phase Motor.	10
Figure 2-7. Linear Motor Layout.	12
Figure 2-8. Force Generation for Linear Motor.	12
Figure 2-9. One DOF Model for Dynamic Stiffness.	17
Figure 2-10. 2 DOF System for Slender Bar.	19
Figure 2-11. Alter and Tsao's Setup (1).	21
Figure 2-12. Basic Structure of Feedback Control System with Disturbance.	27
Figure 2-13. Plant with Measurable Disturbance and Feedforward Controller.	30
Figure 2-14. General Form of the LQG/LTR System.	32
Figure 2-15. Structure of Model-Based Compensator.	34
Figure 2-16. Target Feedback Loop for LQG/LTR.	36

Figure	Page
Figure 2-17. Control Loop Structure for Edmund's Algorithm.	41
Figure 3-1. Shaker/Stage Setup.	44
Figure 3-2. Experimental Setup for Determination of Dynamic Stiffness.	45
Figure 3-3. Static Representation to Determine Bracket Stiffness.	46
Figure 4-1. Block Diagram of Controller and Servo System.	48
Figure 4-2. Plant Block Diagram.	51
Figure 4-3. Motor Mechanical Frequency Response vs. Model Response.	54
Figure 4-4. Experimental Setup to Measure $F/V_{CMD}$ .	55
Figure 4-5. Experimental and Model Response of $F/V_{CMD}$ .	56
Figure 4-6. $Vel/V_{CMD}$ Data for Stage/Coil Mass and Derived Model.	57
Figure 4-7. $Vel/V_{CMD}$ Data for Payload Mass and Derived Model.	58
Figure 4-8. Simulink Model Used to Validate Transfer Function.	60
Figure 4-9. System Step Response vs. Model Step Response.	61
Figure 4-10. Frequency Response Validation of Dynamic Compliance Model.	62
Figure 4-11. System Root Locus Form.	63
Figure 4-12. Plot of Closed-Loop Pole Locations with Varying Position Loop Gain.	65
Figure 4-13. General Root Locus Plot and Second Order Approximation of $\xi$ and $\omega_n$ .	66
Figure 4-14. Layout of Proposed Force Feedforward Controller.	69
Figure 4-15. Controller/Plant Form of Block Diagram.	70
Figure 4-16. Sensitivity and Closed-Loop Principal Gains for One TFL.	73

Figure	Page
Figure 5-1. Dynamic Compliance of Linear Drive with Factory “Tuned” Gains.	77
Figure 5-2. Gain Adjustment to Reduce Resonant Peak of Factory Gains.	77
Figure 5-3. Experimental and Model Response for $\xi=0.05$ .	78
Figure 5-4. Experimental and Model Response for $\xi=0.95$ .	78
Figure 5-7. Target $\omega_n=50$ rad/s.	79
Figure 5-8. Target $\omega_n=100$ rad/s.	79
Figure 5-9. Target $\omega_n=200$ rad/s.	79
Figure 5-10. Target $\omega_n=250$ rad/s.	79
Figure 5-11. Target $\omega_n=300$ rad/s.	80
Figure 5-12. Target $\omega_n=400$ rad/s.	80
Figure 5-13. LQG/LTR Results with $W_n=1000$ , $V_n=1$ and $R=1$ .	81
Figure 5-14. LQG/LTR Results with $W_n=10^6$ , $V_n=1$ and $R=10^{-10}$ .	82
Figure 5-15. LQG/LTR Results with $W_n=10^6$ , $V_n=10^{-6}$ and $R=10^{-15}$ .	82
Figure 5-16. Dynamic Compliance--Force Feedforward Compensation.	84
Figure 6-1. Dynamic Compliance Across Range of $K_I$ .	87
Figure 6-2. Dynamic Compliance Across Range of $K_{POS}$ .	88
Figure 6-3. Dynamic Compliance Across Range of $K_P$ .	88

## NOMENCLATURE

$K_A$	Amplifier Current Loop Gain
$K_{PA}$	Pre-Amplifier Gain (for amplifier commutation)
$K_{CL}$	Current Feedback Gain
$K_F$	Motor Force Constant (N/Amp)
$K_B$	Motor Back EMF (Vs/m)
$K_{POS}$	Controller Position Loop Gain
$K_P$	Controller Velocity Loop Proportional Gain
$K_I$	Controller Velocity Loop Integral Gain
$V_{ff}$	Velocity Feedforward Term in Control Loop
$A_{ff}$	Acceleration Feedforward Term in Control Loop
$F_s$	Sampling Rate—Equivalent to Servo Loop Update Rate
$b$	Damping Coefficient (N/m/s)
$m$	Mass of Moving Portion of Stage and Payload
$N$	Scaling Factor to Convert from Machine Units to Meters
$T_d$	Dynamic Compliance Transfer Function
$C$	Controller Scaling Factor

## SUMMARY

The goal of this research is to modulate the dynamic stiffness profile of a brushless linear DC motor. There is a great deal of research demonstrating the critical role the dynamic stiffness of a machine tool plays in machining processes. Depending on the operation performed and the material of the machined part, different profiles of dynamic stiffness result in varying work piece surface finish, stability margins and process efficiency. Currently, the dynamic stiffness of a machine tool has been strictly dependent on its physical composition. Consequently, the machining process is designed around a machine tool's existing dynamic stiffness. The ability to change the dynamic stiffness of linear drives employed as main feed mechanisms will provide tremendous flexibility to machine tools by allowing the dynamic stiffness to be designed around the desired process.

This research includes performing comprehensive system identification of the motor controller, amplifier and motor system, developing analytical results varying controller parameters to change resonant frequencies and amplitudes of the stiffness profile. Experimental data are obtained for comparison to predicted results. The resultant stiffness of the controlled system is analyzed to determine the relative success of the control system. In addition, several alternative controller designs are developed and analytically studied for possible future implementation.

## CHAPTER I

### INTRODUCTION

The goal of this research is to modulate the dynamic stiffness of a linear brushless DC motor. The ultimate objective in developing this technology is to optimize the dynamic stiffness of a particular machining process by employing linear motors and controls as main feed mechanisms for machine tools.

Currently, the pool of research suggests that the dynamic stiffness of a machine tool has a dramatic effect on machining performance. The ability to shape the dynamic stiffness profile of a machine tool to optimize performance and efficiency for a particular machining process will greatly enhance the flexibility of a given machine. In the past, a process designer could only work with the given dynamic stiffness of the machine being used. If the dynamic stiffness was not appropriate for the process being considered, the option was to perform time-consuming and costly modifications to the machine tool itself or to use a different one altogether.

In recent years the technology of linear direct drive motors has developed adequately and will eventually lead them to serve as mainstream feed mechanisms in machine tools. While there are many inherent advantages to using linear motors in machine tools, being able to shape the stiffness profile of a linear motor could



revolutionize the machining industry by optimizing stiffness for a given process and providing immense flexibility to one machine tool.

Recent research conducted by Alter concluded that dynamic stiffness of a direct drive linear DC motor can be increased by the use of an optimal control scheme (1). This thesis has somewhat different goals and employs somewhat different equipment. First, the present research will implement control with a DC brushless motor. Brushless motors have fewer limitations in terms of mechanical properties and electrical interference that make them more likely to be used in industry. A brushed motor is limited in its speed range by commutation arcing, commutator bar-to-bar voltage, and by brush surface speed (2). Also, the goal of the current research is not only to increase dynamic stiffness at every frequency, but to affect the shape of the dynamic stiffness frequency response. This shaping includes reducing or moving resonant peaks. It is important to distinguish this work from (1) in that no implementation directly involving a machining process was conducted; the linear motor was analyzed apart from the machining process.

### Problem Statement

In this research, a number of tasks were undertaken to show that the dynamic stiffness of a direct drive linear motor can be changed without physically altering any hardware. The following subsections briefly describe the major tasks that were required to successfully complete this research.

### System Identification

Prior to designing or applying any control to a system, one must be able to identify the parameters of the process and obtain a reasonably accurate mathematical model of the system. This research presents a logical and straightforward approach to perform a mathematical system modeling of the controller, motor and amplifier system.

### Model Verification

To ensure that a reasonably good model has been formulated, tests were performed to compare experimental results with those predicted by the model. Such comparisons were undertaken in both the time and the frequency domains.

### Use of Existing Control Structure to Modify Stiffness Profile

Once an accurate model was obtained and verified, tests were conducted to show how selection of control gains on the existing control structure can approximately meet a target shape for the dynamic stiffness profile by altering the magnitude and frequencies of resonant peaks.

### Develop Several Control Schemes for Future Use and Perform Theoretical Analysis

In addition to designing gains for the fixed architecture structure of the motion controller, several other control designs were developed and analyzed for future implementation. Control methods examined used disturbance feedforward methodologies and optimal control design techniques.

## CHAPTER II

### LITERATURE REVIEW/BACKGROUND

In order to provide a background of the system being used, the research goals and related concepts, the following sections briefly preview the theory of linear motors and the mechanical concept of dynamic stiffness. To serve as motivation for the work of modulating dynamic stiffness, current research is cited that demonstrates the importance of dynamic stiffness in the machining process. In addition, examples of the current use of linear drives in industry and research on them are presented. Lastly, to serve as a basis for later sections, general descriptions of the control strategies attempted in this and other related research are presented.

#### Brushless Linear DC Motors

The technology of linear motors has matured rapidly within the last decade. Initially, several points regarding terminology must be clarified as they often cause confusion. Because brushless DC motors must provide a commutated or changing signal to the coil to generate an electromotive force, they are often referred to as AC motors. In both DC and DC brushless motors, the motor produces an electromotive force by the

current it develops acting perpendicular to its magnetic field. To continue developing the force, the electric field has to be kept approximately perpendicular to the magnetic field. The process of changing the current flow orientation in the different motor phases is called commutation. This is the point where DC and DC brushless motors diverge. In DC motors, as the armature moves, current flows to the appropriate coil by means of conductive brushes and commutation bars. In brushless motors, the current is kept perpendicular to the magnetic field by splitting the current into phases based on electronic switching and position sensors.

### Motor Theory

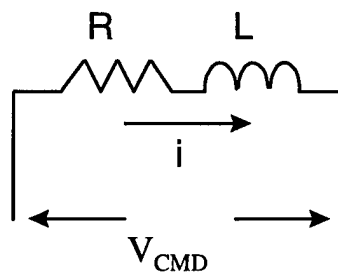


Figure 2-1. Motor Electrical Circuit for Permanent Magnet Motor.

Electrically, a motor coil consists of an inductance and a resistance as shown in Figure 2-1. The differential equation for Figure 2-1 is given by (2-1) where  $V_{CMD}$  is source voltage,  $i$  is current,  $R$  is resistance and  $L$  is inductance.

$$V = iR + L \frac{d}{dt}(i) \quad (2-1)$$

Rearranging and taking the Laplace transform of (2-1), one can obtain the transfer function from voltage input to current output given by (2-2). This transfer function shows how current is developed from a command voltage to the motor.

$$\frac{I(s)}{V(s)} = \frac{1}{Ls + R} \quad (2-2)$$

To understand how the generated current in the coil becomes a force to drive the payload, one must examine basic magnetic theory. If a straight conductor of length,  $\ell$  (in meters), carries a current,  $i$  (in Amperes), through an external magnetic field,  $B$  (in Tesla or Newtons/Amp·m), the force on that current is given by (2-3) (11). The cross product in (2-3) implies that force is maximized by keeping the current ( $i$ ) normal to the magnetic field ( $B$ ).

$$F = i\ell \times B \quad (2-3)$$

To fully understand how the generated force of a motor changes with movement, it is useful to examine its back EMF (electromagnetic force) wave form. When the current source is removed from the coil and it is externally driven at constant velocity across alternating magnetic polarities, an alternating voltage is generated. This voltage is

known as the back EMF and its magnitude is proportional to the coil velocity (3). Figure 2-2 illustrates the concept of an alternating back EMF for a two-pole motor with a single phase. The peak torque per unit of current of a motor (peak force in the case of a linear motor) is achieved when a potential is applied to the coil at the rotor location coinciding with the peak of the back EMF wave form.

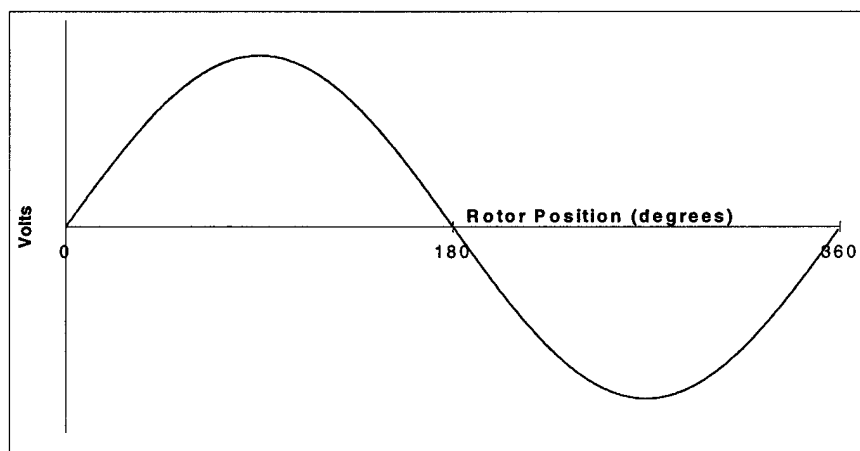


Figure 2-2. Back EMF Wave Form of a Motor Coil.

Figure 2-3 shows the schematic delta configuration for a three-phased coil, spaced  $120^\circ$  apart. Figure 2-4 shows the back EMF seen by each of the three phases ( $\emptyset AC$  indicates the coil between nodes A and C of Figure 2-3) when such a motor is externally driven at a constant speed.

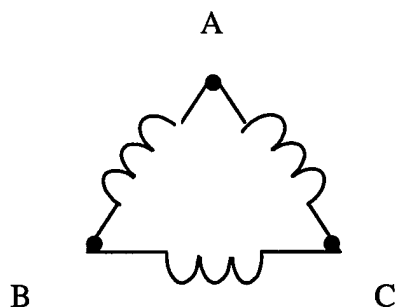


Figure 2-3. Configuration of Three Phase Coil Phased  $120^\circ$  Apart.

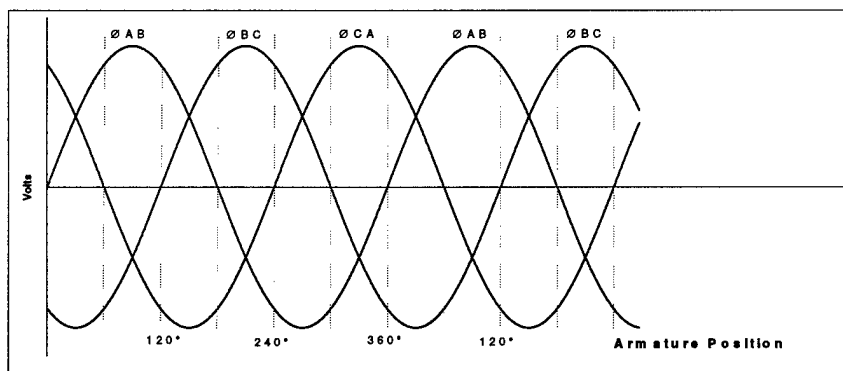


Figure 2-4. Back EMF Wave Form for Three-Phase Winding.

### Commutation

The goal of commutation, based on the brief discussion of the last section, is to keep the current in the motor coil perpendicular to the magnetic field. The windings of the coil are normally phased  $120^\circ$  apart and current must be continually switched to the different motor phases to sustain motion. The commutation points (*i.e.*, the timing of current to the respective phases) for the motor in Figure 2-4 are shown by the shaded

areas in Figure 2-5. From Figure 2-5, it is clear that the generated back EMF and accordingly, the torque produced, vary by 50% from the peak value. This variation is known as torque ripple. To reduce torque ripple, one can double the frequency of commutation to six times per  $360^\circ$  of rotation by using both the positive and negative half of the back EMF wave form as shown in Figure 2-6. The resulting torque ripple is reduced to 13%.

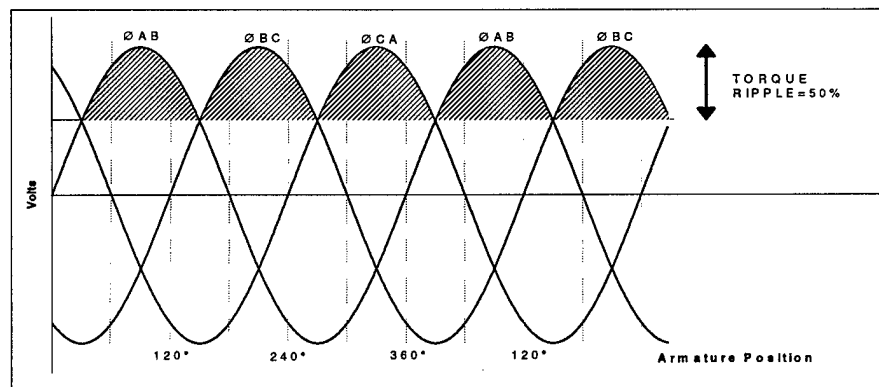


Figure 2-5. 3-Step Commutation Points for a 3-Phase Motor.



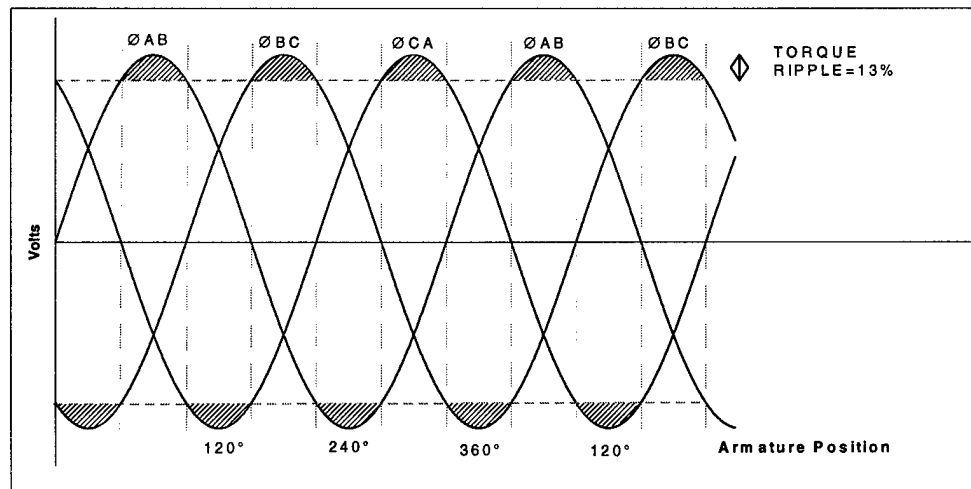


Figure 2-6. 6-Step Commutation Points for a 3-Phase Motor.

The two most common types of commutation are six-step commutation based on Hall Effect sensors and sine wave commutation based on encoder position. In Hall Effect commutation, a circuit board embedded in the coil assembly contains small Hall Effect Device (HED) chips. The HED sensors detect changes in the polarity of the permanent magnet track and switch the motor phases every 60°. Figure 2-6 shows the synchronization for six-step commutation. In sine commutation, a linear encoder used for position feedback is also used to commutate the motor. In general, sine wave commutation provides for smoother motion and less force ripple because the current is continuously kept perpendicular to the magnetic field by updating the phasing each encoder count. Depending on encoder resolution, this is significantly more often than commutation once every 60° as in six-step commutation. On power up, initial phasing is

determined by one Hall state change. Subsequently, the motor phase angle is incrementally advanced with each encoder pulse.

### Modeling Brushless DC Motors

The development of accurate models for brushless DC motors (BDCM) has been the subject of extensive research. The switching of current to the different phases as described above presents a challenge to standard modeling of electromechanical systems. Pillay (4) showed that there are major differences in the models used even between six-step commutation and sine wave commutation for permanent magnet brushless motors. To accurately describe the dynamics of a BDCM that uses sine wave commutation, a second order model is needed, while six-step commutation requires a third order model.

### Linear Motor Description

Linear motors follow the same concepts as the rotary motors described above, except for the fact that the motor is “turned inside out” and “unrolled.” The permanent magnet that is normally the rotor portion of a rotary motor now becomes the stationary track of the linear motor. The coil that is normally the stator or fixed portion of the rotary motor now becomes the “forcer” of the linear motor and moves along the permanent magnet track. Figure 2-7 shows the configuration of the linear motor described here. Figure 2-8 shows the general concept of force generation in a permanent magnet linear motor (5) where the magnetic flux field is represented by dotted lines and the current flows in the direction of the arrows.

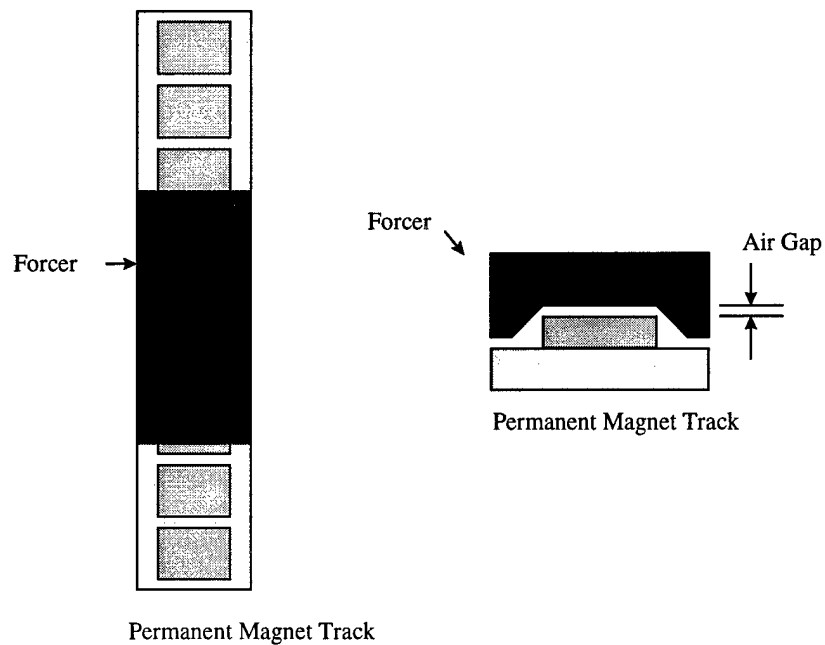


Figure 2-7. Linear Motor Layout.

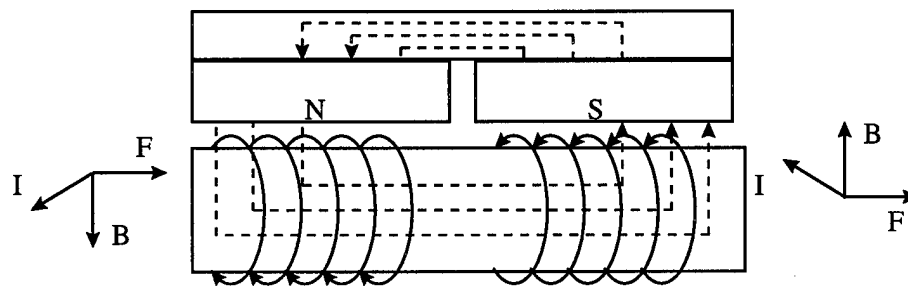


Figure 2-8. Force Generation for Linear Motor.

Some brushless linear motors have fixed coils and a moving magnet. The main advantage of the moving coil is that the stroke length of the motor can be increased by simply adding more permanent magnets, whereas increasing the stroke length of the alternative configurations requires a complete reconfiguration of the windings.

The other obvious difference between linear and rotary motors is that the position of the forcer along the track clearly does not lend itself to measurement in degrees as in a rotary motor. However, in order to split the current into each phase of the forcer windings, position must somehow relate to the phase angle relative to the locations of the north and south poles of the permanent magnets. The magnets are oriented such that a pole change from north to south is at a fixed interval. This fixed distance is equivalent to  $360^\circ$  or one complete "cycle." In this way, with each step of the encoder, the phase angle is updated by a fixed amount.

#### Advantages of Linear Motors in Machining

In view of the general concept of operation of linear motors described in the previous section, one can logically conclude some of the advantages of linear motors in machining. Some advantages of a direct drive are its precise positioning anywhere in the range of travel and the elimination of drive motors, couplings, gear shafts and slides. The elimination of the conventional ballscrew eliminates hysteresis and backlash. Because there are fewer moving parts, there is less hardware to break down and fewer maintenance requirements. The relative accuracy of linear drives as compared to belts, ballscrews and rack and pinions is extremely high. Table 2-1 shows a relative performance comparison of currently available linear motion devices as shown in (6).

Table 2-1. Relative Merits of Linear Motion Devices.

Performance	Units	Linear Motor	Ball Screw	Rack and Pinion	Belt
Accuracy	$\mu\text{m} / 300 \text{ mm}$	0.5	10	50	100
Repeatability	$\mu\text{m}$	0.1	5	25	50
Travel	meter	30	3	30	5
Max Velocity	meter / sec	10	1	2	5
Max Acceleration	g	20	7	5	3
Settling Time	msec / $\mu\text{m}$	10	150	300	500

Because a linear drive motor can be made accurate to within one encoder count, its resolution for positional accuracy is bounded only by encoder resolution (7). They also provide higher velocity and acceleration. In some applications, the use of linear motors has increased velocity by a factor of thirty, increased acceleration by 5 g and exhibited stiffness seven times greater than that of a ballscrew (8).

#### Linear Motor Disadvantages

While there are many advantages associated with the use of linear motors, there are also several drawbacks. One drawback is the high levels of heat generated during use. In a rotary motor, airflow generated by coil rotation carries this heat away. The high levels of heat generated by a linear motor require a method of cooling such as air cooling or heat exchangers. Another disadvantage to linear motors is that the strong permanent magnets attract ferrous dust and chips. Therefore, applications that involve ferrous metals require shielding of the permanent magnets. Lastly, the average cost of linear motors is nearly twice that of conventional linear motion devices.

One of the problems in developing linear motor technology for machine tools is that these drives cannot serve as “drop-in” replacements for other feed mechanisms in

existing machines. Instead, linear motors must be incorporated into the initial design of a machine (8) to provide for the control architecture and space for the somewhat bulky permanent magnets and bearing track. Also, since there is no high-impedance mechanical buffer between the motor and the load such as that between the ballscrew and drive motor, variations in the load can greatly influence performance (9).

#### Uses in Machining Applications

Linear motors have recently received substantial attention in the area of machine tool design. A recent review of machine tool way design (9) called the linear motor a potential replacement for the ballscrew. Because of the many advantages previously mentioned, several machine tool manufacturers, including Ex-Cell-O have turned to the use of linear motors for main feed mechanisms.

The Ex-Cell-O HXC 240 high speed machining center introduced in 1993, employs a linear motor as its main feed drive. The machine was an improvement over conventional machines with respect to acceleration, velocity and accuracy. Consequently, the machining time of similar processes that had been performed conventionally were reduced by 30% on the new machining center. This particular machine has peaked the interest of automotive manufacturers around the world. Ford, General Motors, Mercedes-Benz and Saab have all placed orders or currently use this machining center for various machining applications (10). Machine tool controller manufacturer, Fanuc, recently purchased patents from linear motor producer, Anorad--an indication that broader use in

industry is likely in the near future. Ingersoll-Rand also produces linear motor-based machines for engine block and cylinder block applications.

In general, applications most suited for the use of a linear motor-based machine tool are those with light loads. In order to create enough force for heavier loads, higher machine mass results from more powerful permanent magnets required to develop higher forces. In some applications where higher force levels are required, researchers have used several linear motors in parallel to increase the usable load of the tool (8). Doing so is far simpler when using linear motors, because linking them involves only integration through a control structure. To link other linear motion devices in this way would involve complicated mechanical interaction through gearing.

### Dynamic Stiffness

The previous section serves as a motivation for the use of linear motors in machine tools. This section provides a framework to make the connection between the use of linear motors and dynamic stiffness.

#### Concept of Dynamic Stiffness

A simple model to illustrate dynamic stiffness is a one degree of freedom spring-mass-damper system like the one shown in Figure 2-9 . For the static case, the response of the system is given by the familiar linear relationship of Hooke's Law (11) given by (2-4).

$$F = KX \quad (2-4)$$

At low frequencies, close to the static case, inertial effects of the mass are insignificant, but as the frequency of the excitation force increases and approaches the natural frequency of the system, the displacement of the mass is no longer described by the simple spring relation for static loads. At higher frequencies of the forcing function, the relationship is represented by the differential equation of (2-5).

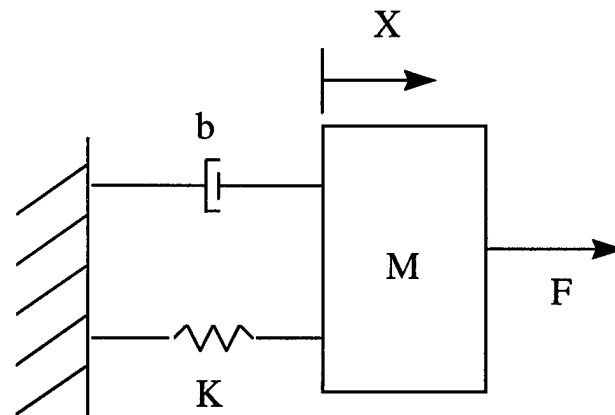


Figure 2-9. One DOF Model for Dynamic Stiffness.

$$M\ddot{x}(t) + b\dot{x}(t) + Kx(t) = F(t) \quad (2-5)$$

In the frequency domain, by taking the Laplace transform of (2-5), the general relation between the force and the displacement is described by:



$$K_D(s)\Big|_{s=j\omega} = \frac{F(s)}{X(s)}\Big|_{s=j\omega} = K_{\text{STATIC}} + bs + Ms^2\Big|_{s=j\omega} \quad (2-6)$$

$$K_D(j\omega) = \frac{F(j\omega)}{X(j\omega)} = K_{\text{STATIC}} + bj\omega - M\omega^2 \quad (2-7)$$

### Dynamic Stiffness Implications on Machining Performance

Dynamic stiffness is the primary issue in designing and analyzing many machining processes. Issues such as stability, surface finish and process efficiency depend primarily on the dynamic stiffness of the tool and work piece.

#### Stability

The most obvious effect of dynamic stiffness on machining performance is that of stability. Dynamic stiffness has a profound effect on stability of a particular machining process. In work conducted by Rivin and Kang (12), a deliberate reduction in tool dynamic stiffness was shown to improve the stability margin of the cutting process for a slender bar. Chatter develops easily when turning slender parts on a lathe because of low stiffness and damping of the system (12). By modeling the system using frequency analysis, the effective stiffness can be determined. Figure 2-10 shows the cutting process as a two-degree-of-freedom (DOF) system.

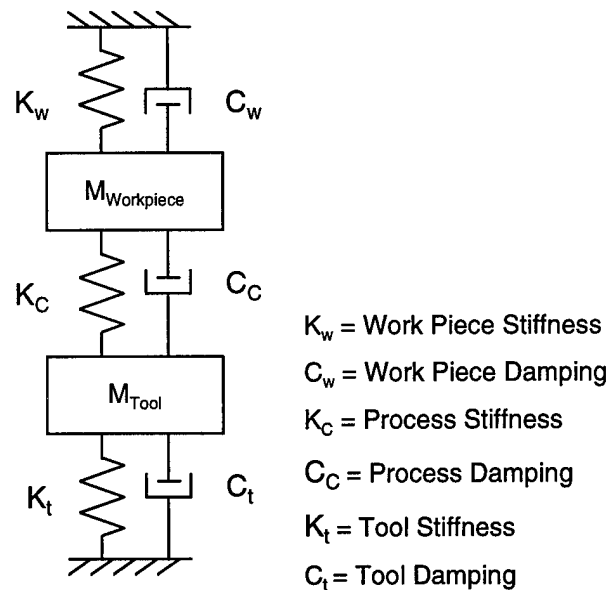


Figure 2-10. 2 DOF System for Slender Bar.

Experimental data showed that chatter vibration frequency changes as the tool moved along the bar and was seen at a maximum when the resulting bar stiffness was minimum. The results of the research showed that once effective cutting stiffness is found, values for optimal effective cutting damping and optimal tool stiffness can be calculated by solving the equations of motion for the two DOF model in Figure 2-10. (12).

Yen and Hsueh (13) have conducted more research on the effect of dynamic stiffness on chatter vibration in inner-diameter cutting. It was shown that chatter vibration could not be suppressed by varying rotational speed. Changing speed affected only the regenerative waviness in the surface finish. One method proposed to suppress chatter was by shifting the resonant frequency to a value outside the operating range. At the  $m^{\text{th}}$  natural frequency,

$$[K]\{x_m\} = \omega_m^2 [M]\{x_m\} \quad (2-8)$$

From (2-8), it may be determined that a change in either  $[K]$  or  $[M]$  yields a different resonant frequency. Looking at (2-7), one can see that such a change also results in a different dynamic stiffness profile. This technique was applied using finite element analysis to design the tool turret at an optimal thickness to yield the best dynamic stiffness.

Research conducted by Elsayed introduced the idea of process damping in the chatter stability equations (14). There is a discrepancy between the stability diagrams normally associated with chatter and experimental observations. Elsayed addresses this difference by a phenomenon known as process damping, that accounts for cutting speed. Process damping yields a force that is generated from the interference between the tool and the previously cut surface. The amount of interference is a function of the tool relief angle and the surface wavelength. Surface wavelength is related to cutting speed by the equation:  $\lambda = \pi d n / f$ , where  $\lambda$  is the wavelength,  $d$  is part diameter,  $n$  is the part speed (rev/sec) and  $f$  is the vibration frequency. The calculation of process damping and the resulting stability diagrams are dependent on the knowledge of the tool/work piece system's dynamic stiffness. Results showed that process damping is, indeed, dependent on cutting speed. In a facing operation, the cutting speed decreases as the tool moves toward the center of the work piece. In the center, the cutting velocity is essentially zero and the system is infinitely stable. The technique may be used to predict the diameter corresponding to the stability limit. The ability to vary dynamic stiffness as the



### Other Measures of Machining Performance

In addition to its effect on stability, dynamic stiffness is a determining factor for machining performance measures such as efficiency and surface finish. It also is rooted in the solutions to practical problems such as tool breakage.

In one case study, a system consisting of a motorized spindle, tooling, part and part-clamping apparatus had a frequent tool-breakage problem (16). Dynamic stiffness of the spindle, tool holder and part was measured. The stiffness of the tool holder was significantly less than that of the part being machined. Because of this differential stiffness, the part was far less susceptible to vibration at resonance than the tool. The investigation indicated that the breakage was being caused by an improper spindle mounting arrangement.

In multi-axis grinding, research by Kurfess and Jenkins has shown that when conducted at resonant frequencies, grinding produced better surface finish in some cases (17). By intentionally machining at resonant frequencies where dynamic stiffness is at a minimum, research showed a decrease in surface roughness for some materials. This is explained by revisiting the well-established correlation between surface finish and minimal force variation. With a reduced stiffness, for each perturbation of the machined surface, the corresponding force perturbation is reduced. By substituting (2-9) into (2-7), one can see that dynamic stiffness is minimized at resonant frequencies.

$$\omega_n = \sqrt{\frac{K_{\text{STATIC}}}{M}} \quad (2-9)$$

Demands for increased efficiency in machining has brought about the concept of “near net shape.” This concept proposes to reduce the amount of work piece material wasted as chips by forging or casting components to their near-finished size. The recent emphasis on such a process has forced machining to be done in one pass, requiring higher depths of cut. Elbastawi and Sagherian have investigated the problem of surface errors associated with such larger depths of cuts on the end-milling of thin-walled sections (18). One of the primary causes of surface errors during such processes is that the dynamic stiffness of the work piece continuously changes as machining progresses. The results obtained showed that the best surface finish was achieved when the milling tooth frequency is equal to the natural frequency of the most significant spindle mode. This frequency corresponds to the lull in dynamic stiffness for the tool.

In the search for higher efficiency in the machining process, Lee and Furukawa (19) have derived a model to determine required parameters in order to perform a plunge grinding roughing operation utilizing full spindle motor power. In order to do this within the constraints of stability, a model was developed to calculate maximum depth of cut and recommended tool stiffness.

The main idea illustrated by the previous section is that, at present, the machining process is designed around the dynamic stiffness of the available tools. For example, consider a case when one desires to optimize surface finish for a given process and

determines that the resonance grinding as described in (17) is to be used. With current technology, the resonant frequency must be selected based on the fixed dynamic stiffness response of the machine tool being used. In the future, one could move the resonant response of the machine tool to employ resonant grinding at a higher spindle speed, optimizing both surface finish and efficiency. As such, the goal of this research is to provide the ability to design the dynamic stiffness around a given desired process.

Having provided background on linear motors and dynamic stiffness as well as motivation for the work of modulating dynamic stiffness, the following sections will address the general tasks associated with the completion of this research, including system identification and general control approaches.

### System Identification

Several methods exist for system identification. One such method is the analysis of a discrete-time input and output stream using an autoregressive moving average (ARMA) model that seeks to minimize the squared error between each actual output and estimated output (20). One problem with this system identification approach in practice is its dependence on the type of input and output being measured. For example, a pure step input theoretically excites all frequency modes and provides adequate frequency information to yield a successful model. In practice, however, a pure step input is not achievable and the resulting response might lack some frequency modes. Therefore, a method using a sinusoidal input to excite the system across a range of frequencies, is

more likely to provide an accurate model for the frequency range of interest. The following section describes how the frequency data are analyzed to obtain a useful model.

The method used to identify the system for this research was to take a set of frequency response data and fit it to numerator and denominator polynomials of known order. Frequency response identification was used because the plant and controller dynamics are of a known order and structure and frequency response data were reasonably simple to obtain. The process of fitting the data is best accomplished by a least squares technique. This approach determines the transfer function polynomials of known order and finds the minimum least squares solution to the polynomial of the same order that fits the given data. The algorithm used is based on the damped Gauss-Newton Method. If a complex frequency response is given by  $h(j\omega)$  at frequencies  $\omega(k)$ ,  $A(\omega(k))$  and  $B(\omega(k))$  are the Fourier transforms of the candidate denominator and numerator polynomials, and  $w_t(k)$  is a weighting of the importance of convergence for each frequency, then the algorithm is iterative to minimize the sum of the squared error as shown in (2-10) (21).

$$\min \sum_{k=1}^n w_t(k) \left| h(k) - \frac{B(\omega(k))}{A(\omega(k))} \right|^2 \quad (2-10)$$

The approach for system identification used in this research resembles that used by Alter inasmuch as each component was isolated and analyzed and later adjusted to fit the frequency response of the overall model (1).



In one approach, system identification and control synthesis are combined into a single problem, using statistical input and output data and spectral analysis (22). This technique results in a "black box" controller over which one has very little control in establishing the order or structure. Since the linear motor used in this research has a fixed-structure controller, the combined approach to system identification and control was not attempted.

Once an adequate model is developed, the next major subtask is the development of a control strategy.

### Control Strategies

A vast amount of research exists in the field of motion control for servo drives. The following sections present several options for motion control and disturbance control. In addition, the limited existing research on dynamic stiffness improvement of linear motors is discussed.

#### Dynamic Compliance Control as Disturbance Rejection

Cutting forces in the machining process can be thought of as a disturbance in the context of position control. The idea of disturbance rejection control has been studied at length since it is a common control criterion for performance. Linear motors are particularly susceptible to disturbances since they have no auxiliary mechanisms to absorb the effects of disturbances such as the gearing found on a ballscrew drive. Because disturbances have a direct effect on a linear drive, often the normal control

routines can command input signals beyond the point of saturation. In one study, a group proposed to employ a preview control for disturbances on a brushless linear motor system to reduce the input commands while still attenuating the effect of disturbances quickly (23).

The description of a generalized plant and controller with a disturbance input is shown by Phillips and Harbor (24) .

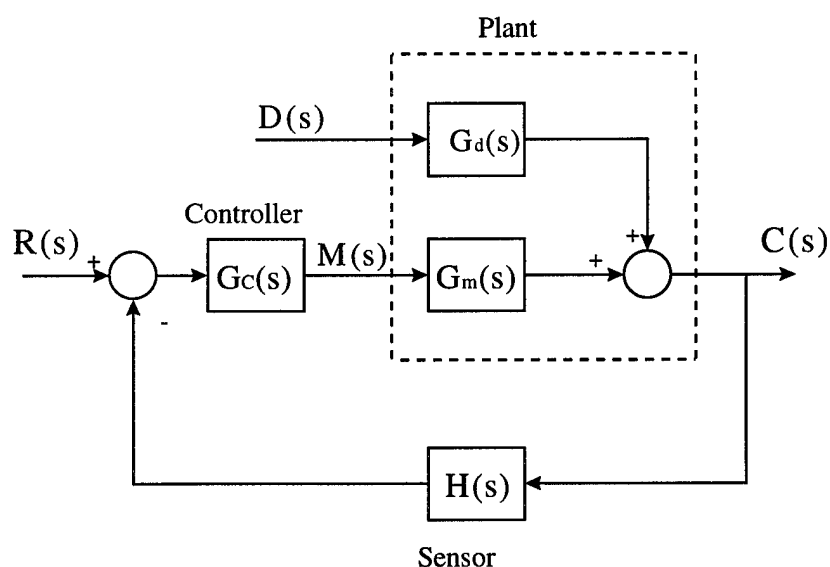


Figure 2-12. Basic Structure of Feedback Control System with Disturbance.

By manipulating the diagram in Figure 2-12, one can obtain the transfer functions from  $D(s)$ , the disturbance input, and  $R(s)$ , the reference input to the output,  $C(s)$ . As expected, Equations (2-11) and (2-12) share a common characteristic polynomial as their

denominator. The output,  $C(s)$  is then, by superposition, additive as shown in Equation (2-13).

$$\frac{C(s)}{R(s)} = T(s) = \frac{G_c G_m}{1 + G_c G_m H} \quad (2-11)$$

$$\frac{C(s)}{D(s)} = T_d(s) = \frac{G_d}{1 + G_c G_m H} \quad (2-12)$$

$$\begin{aligned} C(s) &= T(s)R(s) + T_d(s)D(s) \\ C(s) &= \frac{1}{1 + G_c G_m H} [G_c G_m R(s) + G_d D(s)] \end{aligned} \quad (2-13)$$

In the case of a machining system, dynamic compliance (the inverse of dynamic stiffness) is  $T_d(s)$  (*i.e.*, the output of the system due to disturbance force). To maximize dynamic stiffness, a control scheme should seek to minimize the effect of the disturbance input. This can be accomplished in several ways. One way is to minimize the transfer function from disturbance force,  $F_d$ , to position output in the design of the plant. If the designer can change the parameters of the plant so as to minimize the norm of  $G_d(s)$ , he can reduce the overall magnitude of  $T_d$ . In the case of the linear drive motor, we are starting from an existing system and must accept the resulting dynamic compliance transfer function. A second method for minimizing the effect of a disturbance on the

plant is by increasing the overall loop gain of the system by increasing the gain of  $G_c(s)$ . This concept is best explained by Ogata (25). As  $|G_c G_m H| \gg |G_d|$ , Equation (2-12) approaches zero. Some caution must be used when applying this method. First, as already mentioned, one must make sure that an increase in  $G_c(s)$  does not also increase the gain of  $G_d(s)$  as this would increase the magnitude of the disturbance response. Also, if the system under investigation has a high noise level, large control gains can cause stability problems (24).

The last method is to directly address the disturbance transfer function by developing a disturbance feedforward controller. If the disturbance is measured, then a controller can be developed that will give a command input to the plant to cancel the output produced by the disturbance, before it affects the plant. If the models of  $T(s)$  and  $T_d(s)$  are perfect and no saturation of the components occurs, the result will be to completely cancel the effect of the disturbance. Manipulating Figure 2-13, one can determine the new transfer function,  $T_d(s)$  shown in (2-14). To minimize  $T_d(s)$ , one can determine  $G_{cd}(s)$  to make the numerator of (2-14) equal to zero. The resulting feedforward controller is given by (2-15).

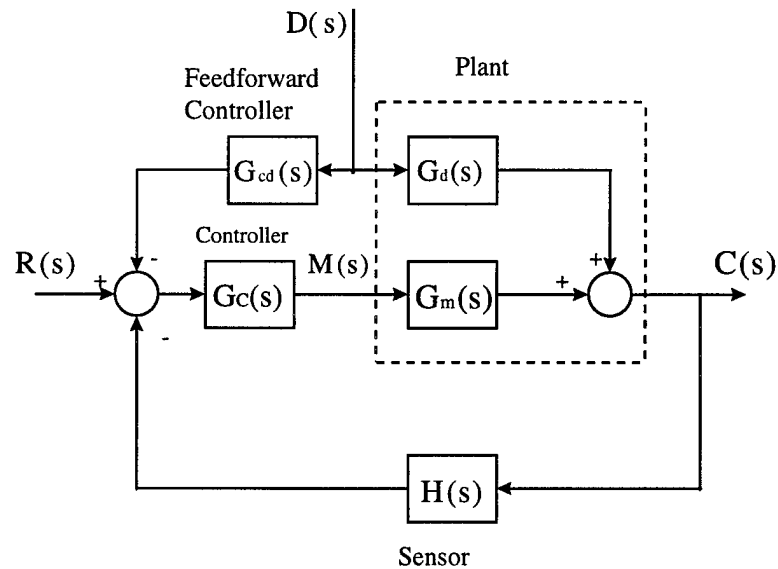


Figure 2-13. Plant with Measurable Disturbance and Feedforward Controller.

$$T_d = \frac{G_d - G_{cd}G_cG_m}{1 + G_cG_mH} \quad (2-14)$$

$$G_{cd} = \frac{G_d}{G_cG_m} \quad (2-15)$$

There are several reasons that preclude  $G_{cd}$  from exactly canceling the effect of the disturbance. Since  $G_cG_m$  is normally a proper system (*i.e.*, the order of the denominator polynomial is of equal or greater order than the numerator polynomial), its inverse is not a physically realizable system. Also, to exactly cancel out the disturbance, the model for  $G_m$  must be exact and the measurement of the disturbance must be noiseless. If such an exact representation was available, no feedback control would be

necessary. Lastly, even if  $G_{cd}$  seems to analytically cancel out the disturbance, the control may require large and rapid changes to the input signal that could saturate the actuator and/or excite higher frequency modes (33). While there seem to be many reasons not to expect the disturbance feedforward control to completely cancel the effect of disturbances, applying such a controller can certainly attenuate the effect of disturbances and should be considered as an early design step.

As mentioned, to employ feedforward control, system disturbance must be measured, adding the expense of a sensor and related hardware. To prevent the requirement of a disturbance sensor, other servo control research (26) developed a disturbance observer based on the motor position output and the current generated at the coil. The observer was then used to provide a feedforward disturbance controller with an estimation of the disturbance.

The emphasis in the above discussion is on feedforward control for a measurable disturbance. Parameter variation and model uncertainty can also be thought of as disturbances to a system. As such, feedforward control can be valuable in compensating for their effects. Uncertainties are obviously unknown, but often have bounds on them over an operating range that allow some degree of analysis (33).

#### LQG/LTR Control

From the derived feedforward scheme described in the previous discussion, the focus is now shifted on a more complicated control scheme known as the Linear Quadratic Gaussian/Loop Transfer Recovery (LQG/LTR) method. The goal of this

method is to design a compensator ( $K(s)$ ) that, when applied to the system plant ( $G(s)$ ) of the general form shown by Figure 2-14, can “recover” a target feedback loop’s performance characteristics arbitrarily well (27).

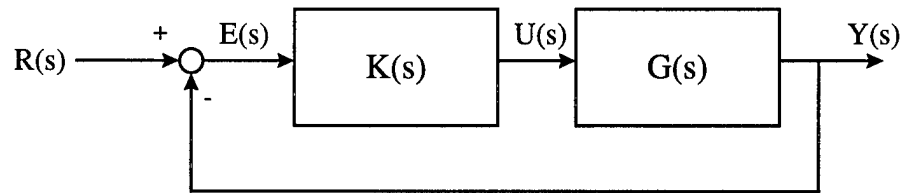


Figure 2-14. General Form of the LQG/LTR System.

The formulation of this method is based on the linear quadratic regulator or LQR control approach, a brief explanation of which follows based on (33). The state space representation of the generalized single-input-single-output (SISO) system (depicted as  $G(s)$  in Figure 2-14) under study is given by (2-16) and (2-17).

$$\dot{\underline{x}}(t) = A\underline{x}(t) + Bu(t) \quad (2-16)$$

$$y(t) = C\underline{x}(t) \quad (2-17)$$

The LQR problem solves the optimal state feedback gains,  $K_C$  that minimize the cost function given by (2-18). The command input vector to the system is given by  $u$  ( $u = -K_C \underline{x}$

with no reference input) and  $z$  is an orthogonal transformation of the state variables ( $z=M\underline{x}$ ). The orthonormal weighting matrices,  $Q$  and  $R$ , penalize state error and large control inputs, respectively.  $K_C$  is given by (2-20) where  $P_C$  is the covariance matrix that solves the Algebraic Ricatti Equation given by (2-21). The Algebraic Ricatti Equation (ARE) is derived by performing a constrained minima problem for (2-18), the details of which are contained in (20) and have been omitted here.

$$J = \lim_{T \rightarrow \infty} E \left\{ \int_0^T (z^T Q z + u^T R u) dt \right\} \quad (2-18)$$

For SISO systems (2-18) reduces to

$$J = \lim_{T \rightarrow \infty} E \left\{ \int_0^T (z^T Q z + R u^2) dt \right\} \quad (2-19)$$

$$K_C = R^{-1} B^T P_C \quad (2-20)$$

$$A^T P_C + P_C A - P_C B R^{-1} B^T P_C + M^T Q M = 0 \quad (2-21)$$



The above description assumes that the outputs of the system are the states (full state feedback). When the states are not available as outputs, one must design an observer to estimate the states from the input and the output. The combined observer controller is often referred to as a model based compensator or MBC (27). The MBC contains a duplicate of the plant model with two feedback loops: one through a matrix,  $H$ , of observer gains and one through matrix,  $G$ , of control gains as shown in Figure 2-15 where  $\Phi(s)$  is the state transition matrix and is given by (2-22).

$$\Phi(s) = (sI - A)^{-1} \quad (2-22)$$

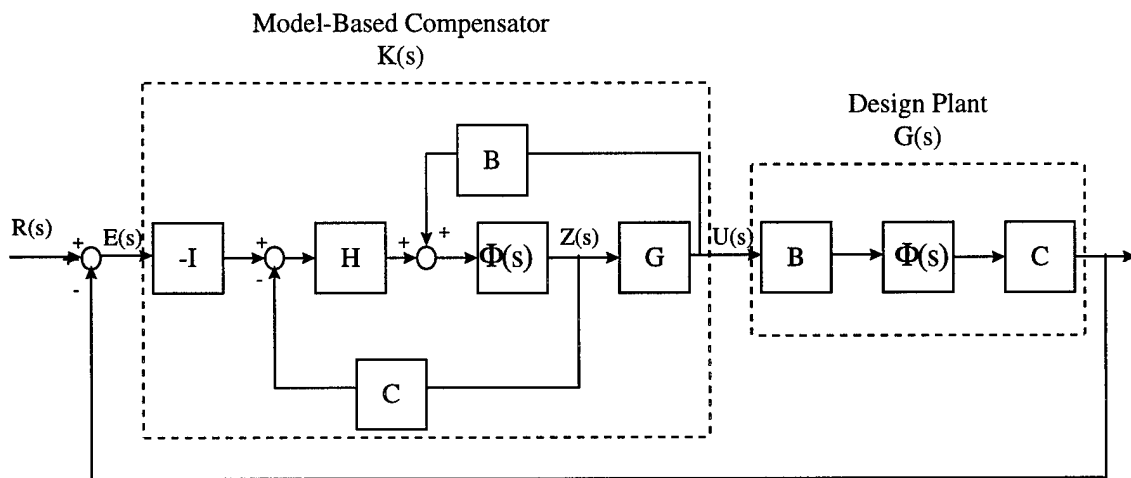


Figure 2-15. Structure of Model-Based Compensator.

A widely used and accepted method of designing optimal observer gains,  $H$ , is Kalman filtering. The dual problem of the LQR problem is the Kalman filter problem

that seeks to minimize the error between the measured and estimated states. The combination of a Kalman filter with an LQR controller is called a linear quadratic Gaussian or LQG controller. A simplified explanation of Kalman filtering is presented based on (33). Assuming a system is given by (2-23) and (2-24), where  $w$  and  $v$  are white processes (*i.e.*, zero mean and uncorrelated with time with a normal or Gaussian distribution) affecting the control and sensor signals respectively. The covariances of  $w$  and  $v$  are assumed to be greater than zero and are given by  $E\{ww^T\}=W$  and  $E\{vv^T\}=V$ . Since the theory is statistically based and actual error between the state and Kalman filter estimate cannot be measured, it is considered optimal on average only (28).

$$\dot{\underline{x}}(t) = A\underline{x}(t) + Bu(t) + \Gamma w(t) \quad (2-23)$$

$$y(t) = C\underline{x}(t) + v(t) \quad (2-24)$$

The Kalman filter gain matrix is given by

$$H = P_f C^T V^{-1} \quad (2-25)$$

where  $P_f$  is determined from (2-26), which is the equivalent algebraic Ricatti equation for the observer error minimization.

$$P_f A^T + A P_f - P_f C^T V^{-1} C P_f + \Gamma W \Gamma^T = 0 \quad (2-26)$$

Although the LQG combines the optimal LQR with the optimal Kalman filter, the resulting controller does not always provide for the best performance or stability (33). The LQG/LTR controller is a special case of the LQG controller that chooses  $G$  and  $H$  of Figure 2-15 in a special way.

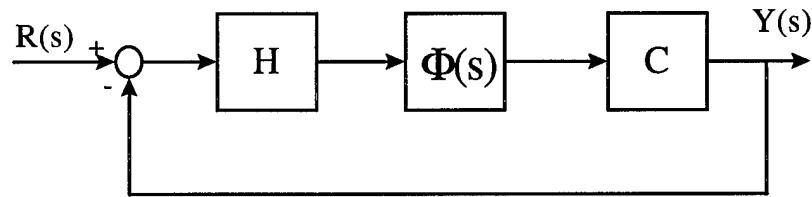


Figure 2-16. Target Feedback Loop for LQG/LTR.

The first step of the LQG/LTR design process is to obtain a target feedback loop as depicted in Figure 2-16 that meets the required stability, robustness and performance characteristics of the closed-loop response. To choose the matrix  $H$ , Kalman filtering techniques have been recommended by (27) and (33). In the Kalman filter synthesis, first, set  $W = W_0 + q\Sigma$ , where  $\Sigma = \Sigma^T \geq 0$  ( $\Sigma=I$  for simplicity) and increase  $q$  arbitrarily toward infinity. By increasing  $q$ , we are “telling” the observer that a greater portion of the output variance is due to state variation and a decreasing proportion to measurement noise (33).

After the target feedback loop design satisfactorily meets performance requirements, the LQR technique is used to choose the matrix of  $G$  in Figure 2-15. First, set  $\Gamma=B$  and  $Q=I$ . By setting  $\Gamma=B$ , the model based compensator essentially generates a stable inverse of the design plant model and several controller poles cancel the plant zeros. For this reason the plant must be minimum phase (*i.e.*, have no zeros in the right half plane) to maintain stability. The last step is to set  $R=\rho I$ , and reduce  $\rho$  arbitrarily close to zero (*i.e.* reduce control cost toward zero). As  $\rho$  approaches zero, the overall transfer function of Figure 2-15 given by (2-27) approaches that of the target feedback loop as shown by (2-28). This is the so-called LTR result and shows that as the control cost is reduced, the output of Figure 2-15 approaches the output of the TFL that was designed to meet specifications (27).

$$\Psi(s) = C(sI - A)^{-1} B G_{\rho} (sI - A + B G_{\rho} + H C)^{-1} H \quad (2-27)$$

$$\lim_{\rho \rightarrow 0} \Psi(s) = C(sI - A)^{-1} H \quad (2-28)$$

While the method described above seems useful in obtaining a desired response, it essentially doubles the order of the system. There are also more sophisticated ways of choosing design parameters  $W$ ,  $\Gamma$  with augmented dynamics to shape the response,

further increasing the order of the system. Several methods have been employed, including (29) to develop a fixed-order LTR controller to reduce complexity and overall system order, while still approximately obtaining the LTR result (*i.e.*, recovering the TFL). In another variation of the method, research conducted by Shafai, used augmented dynamics in the model of the TFL to arbitrarily place the zeros of the plant (30) to achieve the desired response.

Because future implementation of LQG/LTR control on machine tool feed drives will most likely be facilitated by computer, it is useful to assess the LTR result in discrete-time. Bainum and Tan (31) demonstrated that the LTR result is consistent when implemented digitally.

The optimal control approaches described in this section make the presumption that the control designer has the freedom to specify the order and structure of the controller. The methods described in the following section take an alternate stance in optimizing the controller of a fixed structure.

#### Parameter Optimization

The control problem is often constrained to fit a certain existing structure, as is the case in this research--control is constrained to use the existing structure of the Aerotech U-500 motion control card. In the previous sections, discussion focuses on the control of stand-alone controllers without regard to operational constraints or structure. In the methods lumped together under 'parameter optimization,' one can take an existing structure and optimize the adjustable parameters of the structure to most closely match

the desired controller. For example, it was shown in (32) that, in certain cases, the  $H_\infty$  optimal control law can be fit to have the structure of the PID controller commonly found in industry.

### Method of Inequalities

One method of parameter optimization is called method of inequalities. It is based on the idea that system performance is not related to a specific objective value, but must fall between a set of boundaries. For example, an aircraft autopilot system might be constrained to maintain altitude within  $\pm 50$  feet of a target altitude, but its maximum climb rate is between a minimum and maximum value at a given altitude, representing another constraint. In this way design specifications can be presented as a set of inequalities in the form given by (2-29) as shown in (33).

$$|e_i(t)| \leq \epsilon_i, t \geq 0, i = 1, 2, 3, \dots, m \quad (2-29)$$

where each  $e_i(t)$  is a function of time representing plant behavior for one plant variable that must meet the performance constraint of  $\epsilon$ . This method changes the control problem from one of minimization to one of satisfaction of a set of inequalities. This is often a more easily understood concept than other optimal control techniques that design an objective controller. In the event that the objective cannot be met, one can loosen the

restriction of the inequalities for the next iteration rather than redesigning the objective controller as would be the next step in other optimal design techniques (33).

Constraints can result from physical limits of saturation on the input or input rate of change. Limitations can also result if the model being used is valid for only certain parameter values. Nearly any stability or performance measure can be placed in the general form of (2-29). Let the vector of controller parameters in a fixed structure be given by  $p$  with each constraint written in the form of a functional  $\phi(p) \leq 0$ . Suppose a search yields a vector  $p^k$  resulting in a set,  $S^k$ , in which some but not all  $\phi_i(p)$  are met. If the next step of the search finds a set  $p^{k+1}$  for which more  $\phi_i(p)$  are met,  $S^{k+1}$  represents a boundary that is closer to the solution set that satisfies all  $\phi_i(p)$ . The process is repeated iteratively until the set,  $S$  is reached. This concept is referred to in (33) as the 'moving boundaries' process. There are a number optimization algorithms used to perform the search that maximizes the number of  $\phi_i(p)$  satisfied.

#### Edmund's Algorithm

Another method of parameter optimization is called Edmund's Algorithm. In this method, the objective is to make the closed-loop transfer function for the system of Figure 2-17 approach a target transfer function over a specified range of frequencies. The algorithm solves for the numerator coefficients of the controller,  $K$ , in Figure 2-17 (33). Let  $T$  be the closed-loop transfer function actually achieved by  $K$  where

$$T = GK(I + GK)^{-1} \quad (2-30)$$

and  $T_t$  be the target (desired) transfer function. In order to obtain,  $T_t$ , a corresponding  $K_t$ , exists, such that

$$GK_t = T_t(1 - T_t)^{-1} \quad (2-31)$$

It is assumed that  $K$  and  $K_t$  share a fixed and known denominator. The goal of the algorithm then is to determine numerator coefficients of  $K_t$  that minimize the error between  $T$  and  $T_t$ .

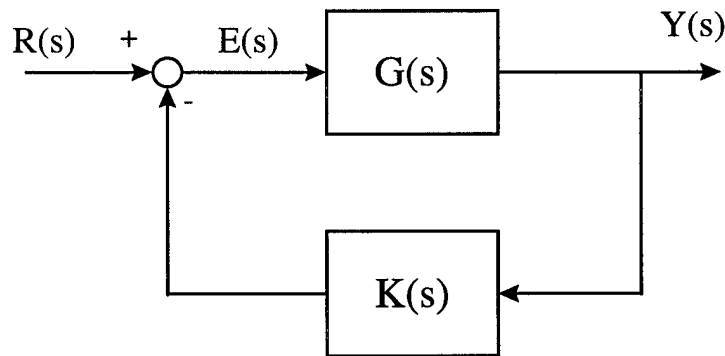


Figure 2-17. Control Loop Structure for Edmund's Algorithm.

This technique was investigated for the current research. However, when the linear motor system was placed in the form of Figure 2-17, the resulting numerator coefficients are not



fully assignable (*i.e.*, only portions of the coefficients are affected by the available controller gains). For this reason, the algorithm was not employed.

### Related Research

The work of changing the dynamic stiffness of a direct-drive linear motor is a fairly new research front. In research conducted at the University of Illinois, Alter employed an  $H_\infty$  control scheme to maximize dynamic stiffness of a DC linear drive used in a grinding application (34). Figure 2-11 shows the configuration for the entire system employed. The  $C_{fb}$  term represents the location of the  $H_\infty$  controller. Alter's approach increased stiffness of the system by a factor greater than two with such a control design over conventional PID control. The goal of Alter's research was to maximize stiffness across the frequency range of operation by minimizing the  $H_\infty$  norm of dynamic compliance.

### Chapter Conclusion

This chapter has provided background information on linear motors, dynamic stiffness and the general concept of system identification and several control schemes. In addition, it provides motivation for the current research in modulating dynamic stiffness of a linear motor for use in machine tools. With this background as a basis, the next chapter briefly describes the instrumentation and equipment used in the research.

## CHAPTER III

### INSTRUMENTATION AND EQUIPMENT

#### Equipment Description

The equipment under test was an Aerotech ALA10076 linear positioning stage with a BLMFI-142A brushless linear drive, a BA-20 amplifier and a Unidex 500 Ultra motion control card. The controller was interfaced with a Pentium 133 MHz processor. The U500 Controller has the capability to perform sine wave commutation to split the current command into its respective phases. In this configuration, the controller passes the current commands for phase A and phase B while phase C is derived by the amplifier. However, since this configuration yields two signals to the plant, the internal commutation was deactivated for some tests in this research in order to allow analysis of a single-ended command input to the plant. The BA20 amplifier has the capability to perform commutation when it has access to the Hall Effect Device sensor signals.

Signal processing for system identification as well as data analysis were accomplished using a DSP Technologies Siglab signal analyzer and Matlab-based software. A Wilcoxon electro-magnetic vibration generator or "shaker" provided force excitation across target frequency ranges.

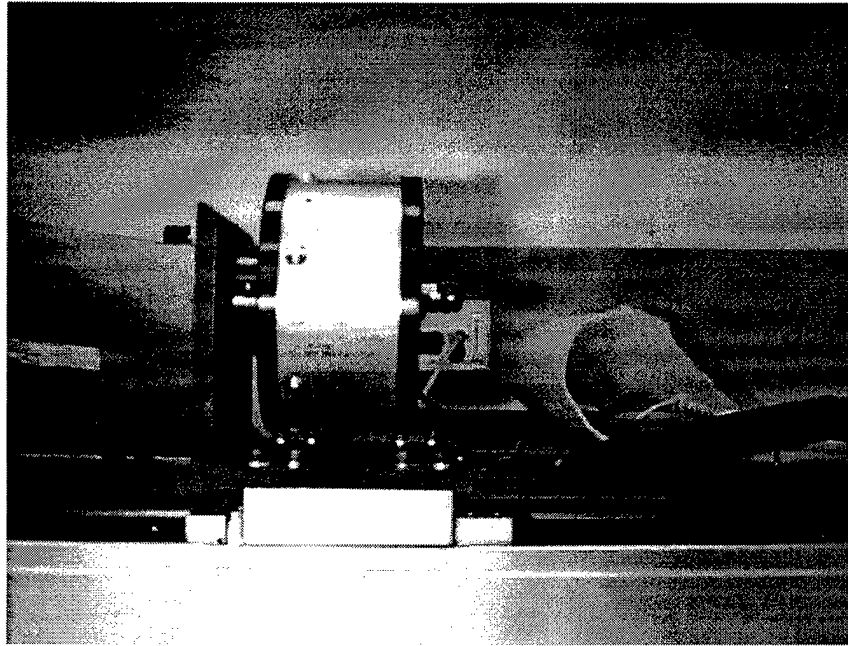


Figure 3-1. Shaker/Stage Setup.

#### Dynamic Stiffness Measurement

The method used to determine dynamic stiffness employed a vibration generator or “shaker.” The shaker contains an outer magnetic portion with a coil traversing a stationary inner portion, on which an accelerometer and force sensor are mounted. Siglab can be set up to output a swept sine wave excitation across a desired range of frequencies to the shaker. The inputs to Siglab for analysis are force (the system input) from the shaker piezo-electric force sensor and either acceleration, velocity or position (the system output).

Since the measurement of dynamic stiffness requires force and displacement, if acceleration or velocity measurements are used, they must be converted to displacement

by an integration. To avoid this integration, displacement can be measured directly by using either an eddy current probe or the linear stage encoder through the controller digital-to-analog converter (DAC). The use of the encoder data was limited by its  $1\mu\text{m}$  resolution, since, at higher excitation frequencies, the shaker does not generate enough force to result in a  $1\mu\text{m}$  displacement of the stage. A subsequent increase in output voltage to the shaker often results in an over-current situation in the motor amplifier. For this reason, the encoder was not usable at higher frequencies (above 200 Hz). On the other hand, in several cases, the magnitude of stage displacement was beyond the measurement envelope of the eddy current probe, precluding its use. In all cases, the use of the appropriate position measurement technique must be determined and applied.

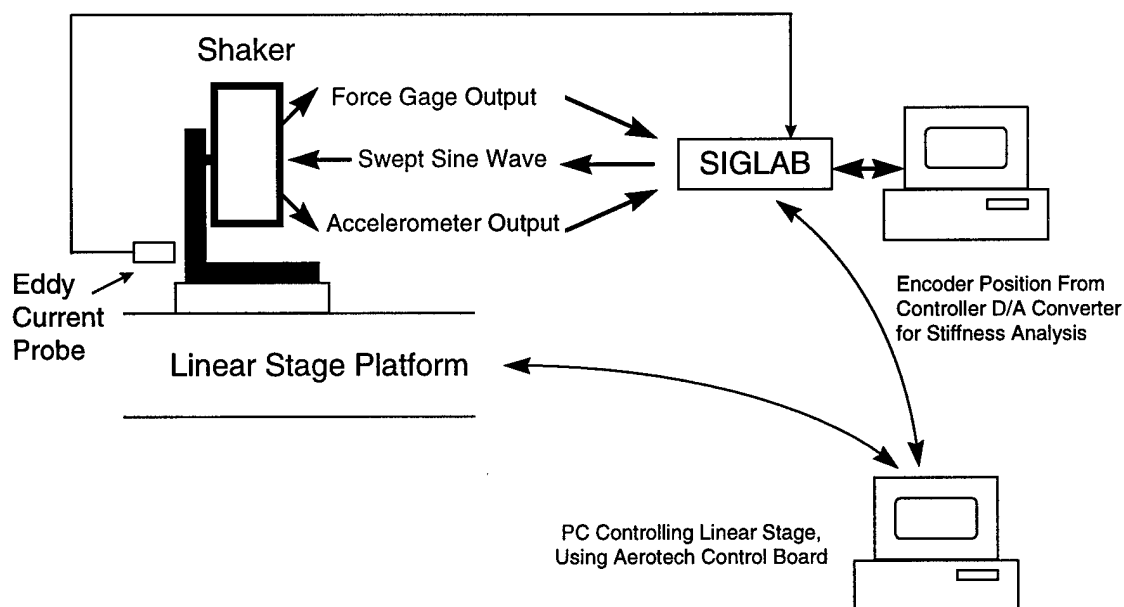


Figure 3-2. Experimental Setup for Determination of Dynamic Stiffness.

Since the shaker vibrates axially from its mounting point, a method of mounting it had to be formulated. To accomplish this purpose, steel L-beam stock was mounted to the slide and the shaker was bolted on the perpendicular portion (See Figure 3-2). To ensure that the bracket was stiff enough for the tests being performed, simple beam calculations were conducted for the static case. The equation for a static cantilevered beam is given by (3-1) as shown in (35). The resulting stiffness for the beam used is  $2.33 \times 10^7$  Newtons per meter—more stiff than most test cases in this research (See Figure 3-3).

$$\delta = \frac{P_a a^3}{3EI} \Rightarrow \frac{\delta}{P_a} = \frac{a^3}{3EI} \Rightarrow \frac{P_a}{\delta} = K_{\text{STATIC}} = \frac{3EI}{a^3} \quad (3-1)$$

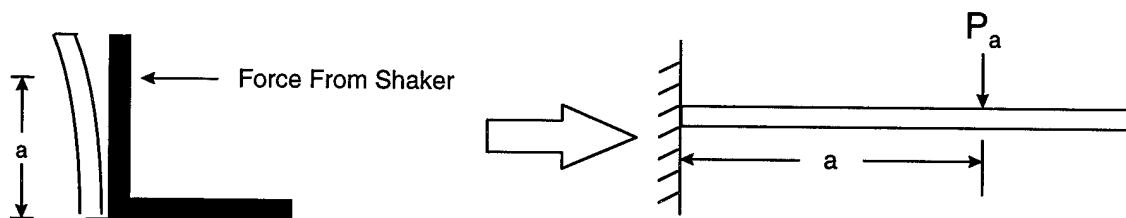


Figure 3-3. Static Representation to Determine Bracket Stiffness.

## CHAPTER IV

### PROCEDURES

To facilitate the goals of this research, procedures were developed and followed for each subtask, from system identification to experimentally shaping the dynamic stiffness. The following section details the procedures used to reach the conclusions of this thesis.

#### System Identification

The first subtask of this research was to conduct comprehensive system identification for the controller, amplifier and linear motor. Figure 4-1 shows the basic structure of the system having two inputs (the command input,  $u$  and disturbance force,  $F_d$ ) and one output (the stage displacement,  $y$ ). The blocks on the left hand portion of the Figure 4-1 are from the controller:  $K_{POS}$  is the position loop gain;  $K_P$  is the velocity loop proportional gain;  $K_I$  is the velocity loop integral gain;  $V_{ff}$  is the velocity feedforward gain;  $A_{ff}$  is the acceleration feedforward gain;  $N$  represents the scaling between meters, on which the plant is based, and machine units that the controller uses and  $F_s$  is the controller servo loop sampling frequency. The remaining blocks are part of the system plant (*i.e.*, the amplifier, coil, and mass).  $K_{PA}$  is the preamplifier circuit of the amplifier (this gain is bypassed when the controller performs the commutation);  $K_A$  is the amplifier current

loop gain;  $K_{CL}$  is the current loop feedback gain;  $L$  and  $R$  are the equivalent motor coil inductance and resistance, respectively;  $m$  is the mass of the moving forcer and payload and  $b$  is the damping coefficient of the mechanical portion of the motor. Of primary concern for the system is its dynamic compliance—that is—the response of the system output displacement,  $Y$ , as a function of  $F_d$ , the disturbance force input. The system dynamic stiffness is the inverse of its dynamic compliance. In this research,  $F_d$  is provided at varying frequencies using a shaker as discussed in Chapter III. During machining,  $F_d$  is generated by the cutting or grinding process itself.

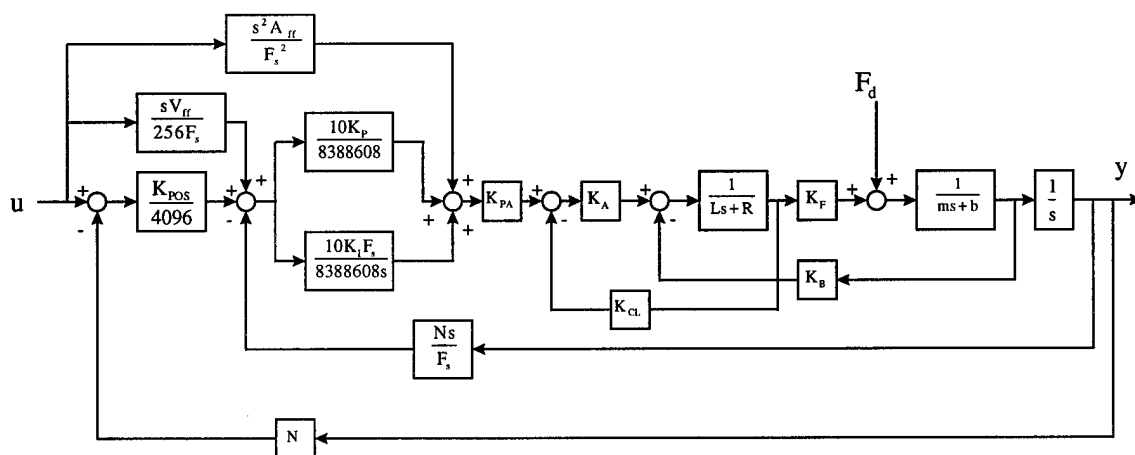


Figure 4-1. Block Diagram of Controller and Servo System.

Many of the variables in Figure 4-1 are provided by factory documentation or were simplistically determined. Table 4-1 lists all parameters as provided and later determined for use in the model.

Table 4-1. System Parameter Values.

Parameter	Supplied Value	Model Value	Units
Mass, Positioning Stage/Coil/Encoder	1.571	1.571	kg
Mass, Shaker Bracket /and Mounting Hardware	3.800	3.800	kg
Mass, Shaker and Bolt	3.133	3.133	kg
Motor Coil Inductance, L	0.0044	0.0044	H
Motor Resistance (25° C), R	11.0	12.8	Ohms
Motor Resistance (150° C), R	16.7	N/A	Ohms
Motor Force Constant, $K_F$	19.6	19.6	N/Amp
Motor Back EMF, $K_B$	15.8	1.4	V/m/s
Sampling Frequency, $F_s$	4000.0	4000.0	Hz
Amplifier Gain, $K_A$	10.0	10.0	
Pre-Amplifier Gain, $K_{PA}$	N/A	0.594	
Amplifier Current Feedback Gain, $K_{CL}$	N/A	0.133	

### Controller

The first section of Figure 4-1 is the existing controller structure. The controller used for this research is an Aerotech Unidex 500 Ultra Motion Control Card. It is incorporated into a Pentium Processor PC through which commands are passed and feedback monitored. The block diagram provided by the manufacturer (see Figure 4-1) depicts a non-standard representation of the controller that combines discrete and continuous notation. Such a non-standard approach makes control analysis and design difficult for this system. Sampling frequency, denoted as  $F_s$  in Figure 4-1, which is normally seen as  $1/T$  (sampling interval), is associated with the discrete time representation using the discrete “z” operator or the “w” operator for its bilinear transformation. However, in this case,  $F_s$  is shown in the same diagram as the continuous



domain Laplace operator “s.” Since a digital computer carries out the control process, the block diagram should be represented in the discrete domain. Because no data or insight were available on the manufacturer’s rationale for such a representation, the structure of the controller block diagram was taken at face value in the continuous-time domain. Because frequencies considered for this research were capped at 200 Hz and the controller sampling frequency is 4 kHz, the system has been represented and controlled in a continuous-time framework. The Nyquist sampling criterion requires that the sampling frequency exceed operational frequencies by at least a factor of two. This requirement has been exceeded by a factor of ten. Future work that implements control at higher frequencies should consider and accurately model the discrete effects of the control system.

### System Plant

The plant consists of the amplifier, motor coil and mechanical mass system. The amplifier converts a current command voltage into a current generated at the motor coil. The motor electrical portion consists of the coil itself where the current generated in the presence of the magnetic field of the permanent ferrous magnets creates an electromotive force. The electromotive force produced by the coil is then applied to the motor mechanical portion of the system that consists only of the coil mass, stage and payload as well as damping elements. Since the mechanical portion of the motor has no resistance other than friction when the coil is de-energized, static stiffness is assumed to be zero.

Figure 4-2 shows the structure of the plant where  $F_d$  is the disturbance force applied to the motor mechanical block.

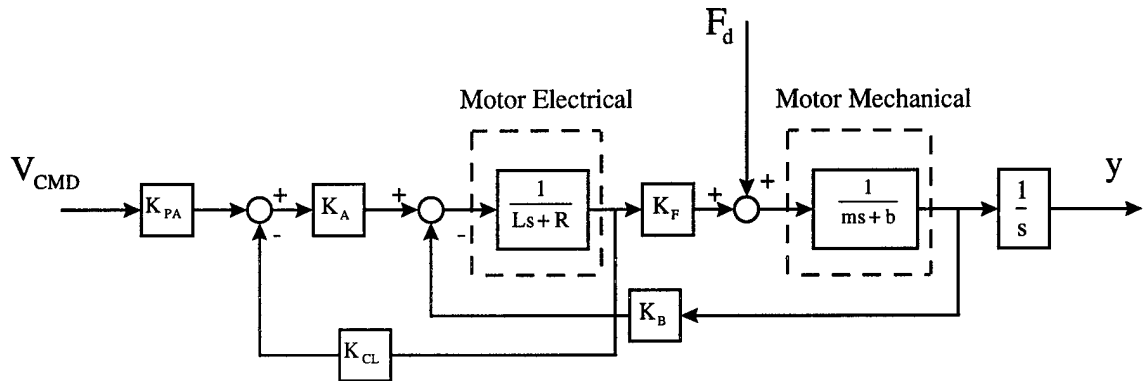


Figure 4-2. Plant Block Diagram.

Because the typical approach to modeling brushless motors is very complex, and would preclude standard analysis methods, several simplifying assumptions were made in developing the model for this research. In general, a brushless motor is a non-linear system because of the switching of current flow to multiple phases. In this research, the system is modeled after a DC motor--as if only one phase was in the core. In other words, the three-coil core is modeled as one equivalent resistance and inductance. This assumption provides a good model for dynamic compliance as results verify. One of the reasons why the model is valid for this application is the length of travel during testing is limited, resulting in small motor phase angle changes.

Identification of the plant presented a unique problem in the context of the brushless DC motor. In the standard configuration, commutation is performed by the

controller itself and requires encoder feedback. Since encoder feedback is required for commutation, open-loop data cannot be obtained independent of the controller. The configuration was later modified to allow the amplifier to perform rudimentary six-step commutation, permitting an alternate method of plant identification.

The first approach was to assemble the system depicted in Figure 4-2 in sections. As a base-line for the system, all parameters published by the manufacturer were assumed to be accurate. Frequency domain curve fitting was then used to modify several parameters to refine the model. The resulting parameters are listed in Table 4-1. The first section of the plant to be analyzed was the motor mechanical portion. Analysis of frequency response data from force excitation input to position output provided a first estimate of the motor mechanical parameters. Tests were performed with the coil de-energized. The initial tests were conducted up to 2 kHz to ensure the overall shape of the response was captured. Force input data were provided by the shaker and its force measurement was read from the shaker's integrated piezo-electric sensor. Measuring position presented another challenge. Since the coil was de-energized, the positioning stage slides freely without any feedback to keep it in a position envelope. For this reason, an eddy current probe was ruled out because of its small measurement envelope. Another alternative was to use the digital-to-analog converter (DAC) of the controller to send a voltage proportional to the number of machine steps as detected by the position encoder. This signal worked well at lower frequencies, where displacement was large—on the order of 10 to 500  $\mu\text{m}$ . However, at higher frequencies, the displacement of the stage was less than the 1- $\mu\text{m}$  resolution offered by the optical encoder. As a solution, low

frequency data were taken from 3 Hz to 200 Hz using the encoder and DAC to measure position output and from 200 Hz to 2 kHz, displacement data were derived using acceleration measurements. Since acceleration is the second derivative of position, a double integration was necessary to obtain position. The integration is performed in the Laplace domain by setting  $s=j\omega$ . Equation (4-2) shows how displacement data were obtained from acceleration. Multiplication by  $e^{j\pi}$  has the effect of reversing the phase by  $180^\circ$  which is the same as multiplication by -1.

$$X(s) = \frac{a}{s^2} \Big|_{s=j\omega} = -\frac{a}{\omega^2} = \frac{a}{\omega^2} e^{j\pi} \quad (4-2)$$

Using a Matlab routine, developed for the purpose, low frequency data were then combined with the higher frequency data and an overall response was obtained. A least squares fit of the combined frequency response data to a second-order system became the initial model. The initial model was then modified using the actual mass of the system and setting the damping coefficient to best fit the actual response. Figure 4-3 shows the comparison of the derived model and the actual data.

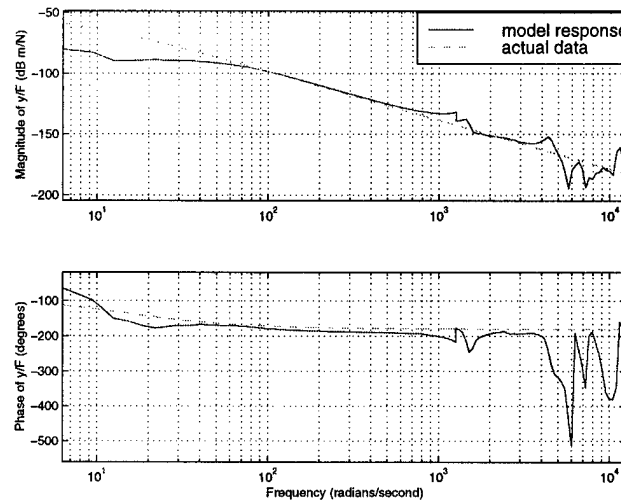


Figure 4-3. Motor Mechanical Frequency Response vs. Model Response.

The next step was to refine the sections of the overall plant shown in Figure 4-2 at lower frequencies. First, the amplifier was set up in the current command configuration to perform rudimentary six-step commutation based on the Hall signals sent from the stage. The next block to be tested was the transfer function from current command input at the amplifier to force output of the stage given by (4-3).

$$\frac{F}{V_{CMD}} = \frac{K_{PA} K_A K_F}{Ls + R + K_{CL} K_A} \quad (4-3)$$

To facilitate this test, the stage was attached to a bracket and an anchored strain gage force sensor. The stiffness of the strain gage ( $1.985 \times 10^5$  Newtons/m) is such that the  $\approx 20$ -Newton force generated by the motor yields only a .1 mm displacement. In view

of this small displacement and the low frequency range used, the inertial effects of the payload mass were ignored for these particular tests. In addition, because velocity was limited by the small length of travel to activate the strain gage, the generated back EMF was also neglected. Force was measured from the strain gage as the output and analyzed with the voltage input provided to the motor amplifier by Siglab. The experimental setup is shown in Figure 4-4.

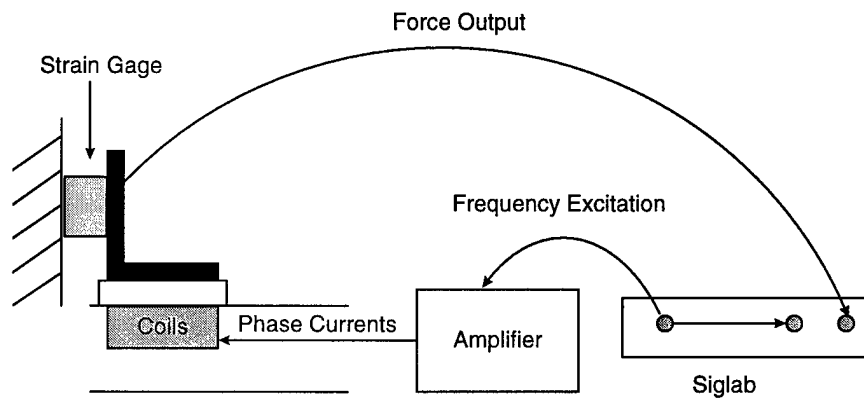


Figure 4-4. Experimental Setup to Measure  $F/V_{CMD}$ .

Figure 4-5 shows experimental data and the model response for  $F/V_{CMD}$ . Agreement between the data and the model is reasonable. Note that only low-frequency data (<35 Hz) is taken to verify the parameter values in (4-3). The low frequency data is sufficient for this purpose and data at this range is unaffected by the poor frequency response of the strain gage force sensor. Static tests would have been less accurate since coil dynamics have a derivative term with respect to current (See Equation (2-1) ).

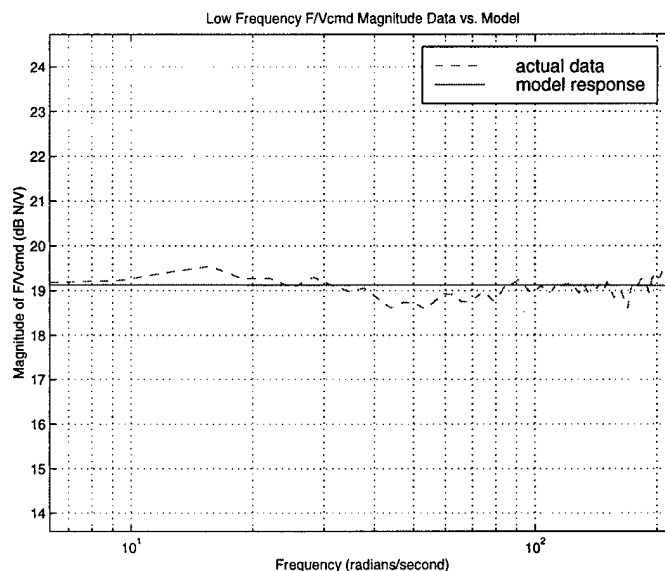


Figure 4-5. Experimental and Model Response of  $F/V_{CMD}$ .

Next, the Siglab provided a current command to the input of the plant and measured the velocity (from the controller DAC) of the stage as the output of the plant. Since the feedback was not connected to the current command in any way, the system was operating open-loop, presenting a potential problem with stability. Since the position is in no way maintained, the stage moved freely, and in an irregular fashion. However, since current command inputs could be kept very small and were random across the frequency range of interest, the range of stage movement remained small. This test was performed once with only the stage and coil mass and once with the shaker and mounting bracket. The tests were conducted for both values of mass to verify the assumption that the different normal forces on the bearing slide due to payload mass affect the damping coefficient of the motor mechanical block. The transfer function from current command

to velocity output derived from manipulation of Figure 4-2 is given by Equation (4-4). A least squares fit was performed using Matlab to fit the data obtained in these tests. The least squares model was then used to solve for reasonable parameters in the system by relating the coefficients of the characteristic polynomial to those given by (4-4). Figure 4-6 and Figure 4-7 show the resulting models compared to the data taken for each mass case.

$$\frac{Vel}{V_{CMD}} = \frac{K_{PA} K_A K_F}{mLs^2 + (m(R + K_{CL} K_A) + bL)s + (R + K_{CL} K_A)b + K_F K_B} \quad (4-4)$$

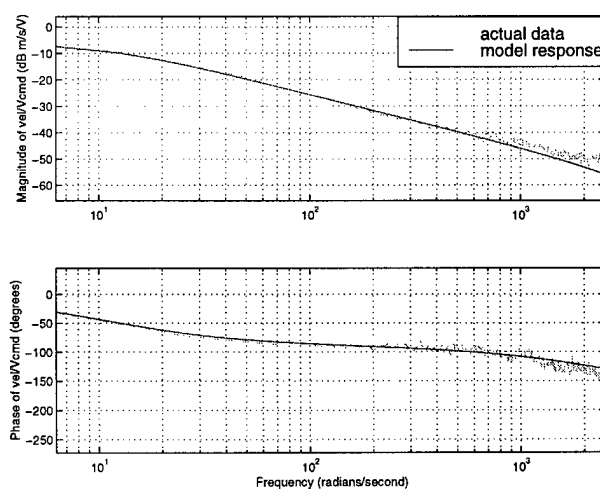


Figure 4-6. Vel/V<sub>CMD</sub> Data for Stage/Coil Mass and Derived Model.



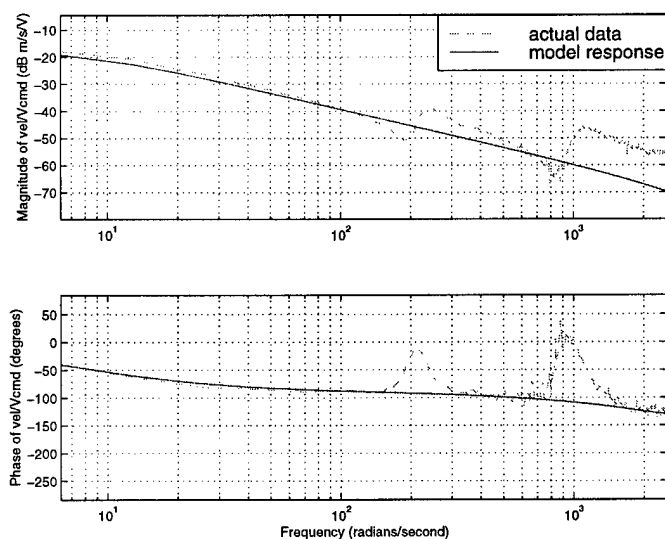


Figure 4-7. Vel/ $V_{CMD}$  Data for Payload Mass and Derived Model.

Once all of the components of the system were determined, block diagram manipulation of Figure 4-1 was accomplished to determine the transfer functions from position command input ( $u$ ) and from disturbance force input ( $F_d$ ) to position output ( $Y$ ). The resulting transfer functions are given by (4-5) and (4-6), where  $C$  is a constant from the on-board scaling of the controller and is equal to  $3.436 \times 10^{10}$ . Naturally, both transfer functions share a common characteristic equation (denominator polynomial) and by the principle of superposition, the output is additive as shown in (4-7).

$$\frac{Y(s)}{U(s)} = \frac{s^3 \left[ C \frac{1}{F_s} K_{PA} K_A K_F A_{ff} \right] + s^2 [160 K_P K_{PA} K_A K_F V_{ff}] + s^4 CLmF_s + s^3 [CF_s (bL + m(R + K_{CL} K_A))] + s [10 K_{PA} K_A K_F F_s (K_P K_{POS} + 16 K_I V_{ff})]}{s^2 [CF_s (b(R + K_{CL} K_A) + K_F K_B) + 40960 K_{PA} K_A K_F K_P N] + 40960 K_{PA} K_A K_F K_P N + 10 K_I K_{POS} K_{PA} K_A K_F F_s^2} \dots \quad (4-5)$$

$$\frac{s [10 K_{PA} K_A K_F NF_s (4096 K_I + K_P K_{POS})] + 10 K_{PA} K_A K_F K_{POS} K_I F_s^2}{s [10 K_{PA} K_A K_F NF_s (4096 K_I + K_P K_{POS})] + 10 K_{PA} K_A K_F K_{POS} K_I F_s^2}$$

$$\frac{Y(s)}{F_d(s)} = \frac{s^2 [CLF_s]}{s^4 [CLmF_s] + s^3 [CF_s (bL + (R + K_{CL} K_A) m)] + s [C(R + K_{CL} K_A) F_s]} \dots \quad (4-6)$$

$$\frac{s^2 [CF_s (b(R + K_{CL} K_A) + K_F K_B) + 40960 K_{PA} K_A K_F K_P N] + 40960 K_{PA} K_A K_F K_P N + 10 K_I K_{POS} K_{PA} K_A K_F F_s^2}{s [10 K_{PA} K_A K_F NF_s (4096 K_I + K_P K_{POS})] + 10 K_{PA} K_A K_F K_{POS} K_I F_s^2}$$

$$Y(s) = \frac{Y(s)}{U(s)} U(s) + \frac{Y(s)}{F_d(s)} F_d(s) \quad (4-7)$$

### Transfer Function Validation

Having derived (4-5) and (4-6) and substituting values of the parameters, the next logical step is to verify the model using both time domain and frequency domain comparisons to experimental data. The Aerotech controller does not allow the user to supply external control inputs at high enough frequencies to perform a frequency response analysis of the model for  $Y/F_d$ . Therefore, to validate (4-5), a step position



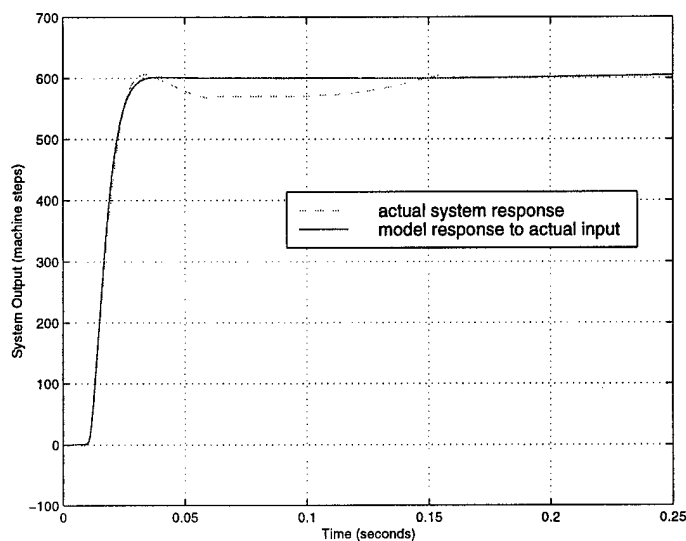


Figure 4-9. System Step Response vs. Model Step Response.

Frequency response tests using the shaker for force input and measuring position output using the U500 DAC were conducted to validate (4-6).

Figure 4-10 shows the predicted shape of the compliance curve and the actual shape obtained. Having obtained a reasonable model of the entire system, the next step is to explore several methods to control dynamic stiffness.

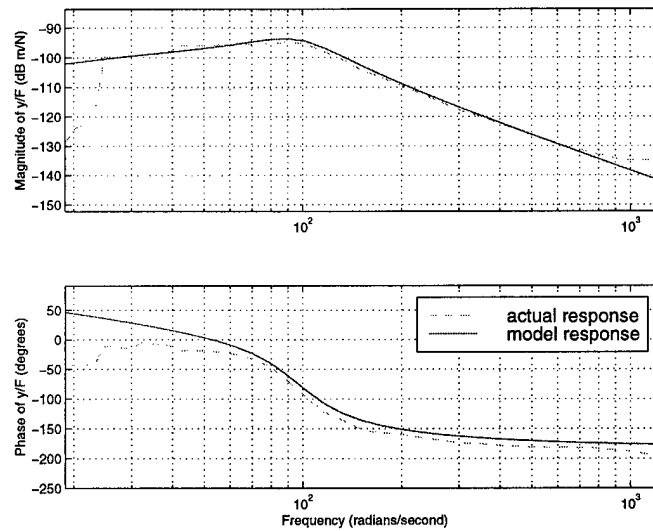


Figure 4-10. Frequency Response Validation of Dynamic Compliance Model.

### Control Strategy

The following section describes the use of several methods to control the dynamic compliance of the system under study. At present, the only method for which experimental results were obtained is that of varying the gains of the existing control structure based on the model developed in the previous section. The other methods are presented as a basis for future work. Analytical results using these methods are presented in Chapter V.

### Choosing Controller Gains to Change Natural Frequency and Damping Ratio

The first method to control dynamic stiffness is by selecting the existing control gains to meet a target shape. In order to choose controller gains to change damping ratios and resonant frequencies of the compliance response, Matlab code was developed to plot the closed-loop poles for a range of each adjustable control gain while others were fixed at nominal values. To facilitate the use of the “rlocus” command in Matlab, the denominator of Equation (4-6), had to be manipulated into the root locus form. The root locus form of a generalized system is shown in Figure 4-11 (24). The transfer function of Figure 4-11 is given by (4-8) and its root locus consists of the denominator roots as  $K$  is varied between 0 and  $\infty$ .

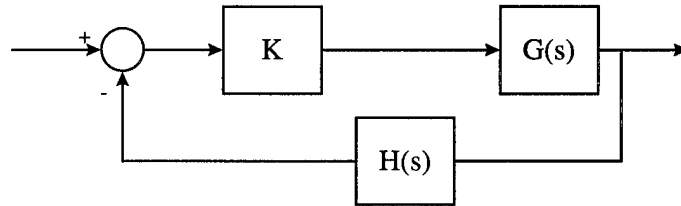


Figure 4-11. System Root Locus Form.

$$\frac{KG(s)}{1 + KG(s)H(s)} \Rightarrow \frac{K \frac{N(s)}{D(s)}}{1 + K \frac{N(s)}{D(s)} H(s)} \Rightarrow \frac{KN(s)}{D(s) + KN(s)H(s)} \quad (4-8)$$

With the goal of varying each of the adjustable gains in (4-6), manipulation is conducted to place the denominator in the form of (4-9) for  $K_{POS}$ ,  $K_P$  and  $K_I$ .

$$D(s) + KN(s) = 0 \quad (4-9)$$

For example, for  $K_{POS}$  (assuming unity gain feedback), the denominator of (4-6) becomes

$$D(s) + K_{POS}N(s) = 0 \quad (4-10)$$

where

$$\begin{aligned} D(s) = & s^4[CLmF_s] + s^3[CF_s(bL + (R + K_{CL}K_A)m)] + \dots \\ & s^2[CF_s(b(R + K_{CL}K_A) + K_FK_B) + 40960K_{PA}K_AK_FK_PN] + \dots \\ & s[40960K_{PA}K_AK_FNF_SK_I] \end{aligned} \quad (4-11)$$

and

$$N(s) = s[10K_{PA}K_AK_FNF_SK_P] + 10NK_{PA}K_AK_FK_IF_s^2 \quad (4-12)$$

This tool is useful in choosing a desired damping ratio for a given set of control gains. For example, by varying the value of the position loop gain,  $K_{POS}$ , one can see from Figure 4-12 that damping is decreased with increasing gain and that, eventually, the

poles cross the imaginary axis and become unstable. Inspection of Figure 4-12 shows that the scaling of the real and imaginary axes is not square as would be expected from a typical root locus plot. The figure has been magnified and its scaling adjusted to fill the available plot area for visualization of root behavior. Using the “rlocfind” function of Matlab, one can easily determine the value of  $K_{POS}$  for any given position on the root locus plot. This feature is especially useful in determining the stability limit for each gain by determining the value of gain at the imaginary axis crossing point.

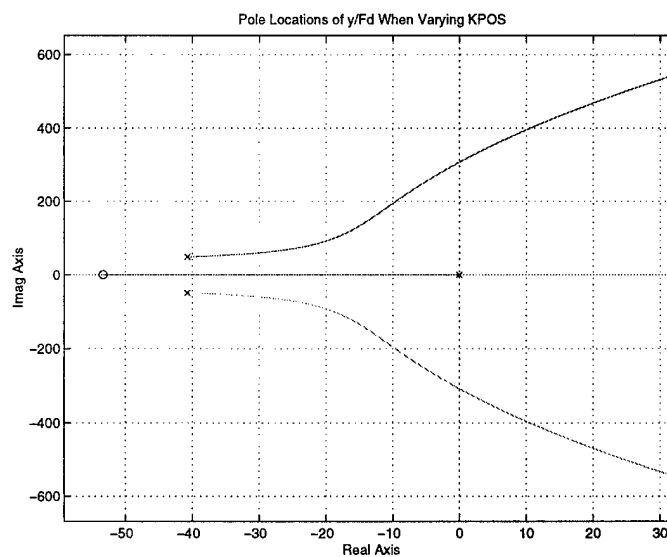


Figure 4-12. Plot of Closed-Loop Pole Locations with Varying Position Loop Gain.

(Note: Fast Pole at  $s \approx -3000$  is not shown in this plot).

To determine values of gain in a more systematic manner and generate a target frequency response, several assumptions were made to simplify analysis. Although the



closed-loop transfer function for dynamic compliance is fourth order, its transient frequency response is assumed to be dominated by the two complex conjugate poles in Figure 4-12 (24). Second order approximations based on the two complex poles were used to determine damping ratio,  $\xi$  and the corresponding natural frequency,  $\omega_n$ , at which the resonant peak approximately occurs. This assumption was used only in calculating controller gains to meet approximate values for  $\xi$  and  $\omega_n$ . The full fourth-order model was used to determine the actual locations of the poles as well as the frequency responses of the model.

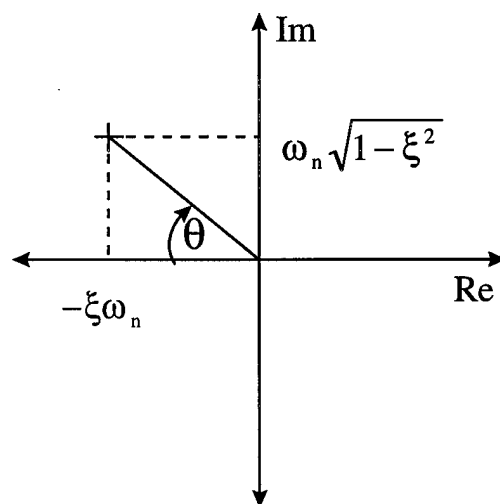


Figure 4-13. General Root Locus Plot and Second Order Approximation of  $\xi$  and  $\omega_n$ .

Figure 4-13 shows how  $\omega_n$  and  $\xi$  are calculated using the second order approximations of (4-13) and (4-14).

$$\tan \theta = \frac{\omega_n \sqrt{1 - \xi^2}}{\xi \omega_n} \Rightarrow \xi = \frac{1}{\sqrt{\tan^2 \theta + 1}} \quad (4-13)$$

$$\text{Re}(\text{pole}) = \xi \omega_n \Rightarrow \omega_n = \frac{\text{real}(\text{pole})}{\xi} \quad (4-14)$$

Knowledge of approximate values of  $\omega_n$  and  $\xi$ , (based on the second order approximation) gives an indication of the resonant frequency and the relative amplitude of the resonant peak, respectively. This approximation works reasonably well in predicting the resonant frequency of dynamic compliance as demonstrated in Chapter V. A recursive Matlab routine, based on the assumption of complex pole dominance was developed to find a set stable gains that moves the complex poles to most closely achieve the desired damping ratio or resonant frequency. The algorithm used is similar to that described by the method of inequalities in Chapter II.

It is possible to predict the regions of the root locus for which the assumption of complex conjugate pole dominance is valid. In general, the poles that are closest to the imaginary axis dominate a response, because they correspond to transient response terms that decay more slowly (25). Therefore, when the complex conjugate poles are closer to the imaginary axis than the third pole on the real axis, they will dominate the response. Using the same analytic tool developed to generate Figure 4-12, ranges of controller gains were determined which resulted in pole locations where the real-axis pole is further from

the imaginary axis by a factor of 3. The selection of this relative factor is arbitrary and is chosen only to provide an approximate range for the validity of the second order assumption. The ranges determined for validity of the second-order approximation are given in Table 4-2.

Table 4-2. Controller Gain Ranges for Validity of 2nd-Order Approximation.

Range for 2 <sup>nd</sup> -Order Approximation Validity	
$K_{POS}$	>200
$K_I$	>2400
$K_P$	30000-140000

#### Force Feedforward Controller

To provide an alternative control structure that may be implemented with minimal change to the existing setup, the following disturbance feedforward control concept was developed, where  $K_{SEN}$  is the force transducer sensitivity and  $G_{FF}$  is the force feedforward controller.

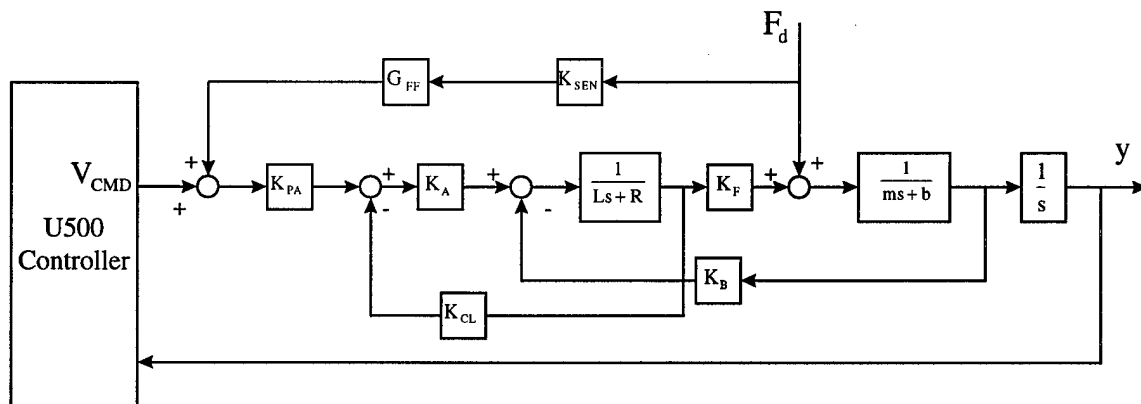


Figure 4-14. Layout of Proposed Force Feedforward Controller.

To effectively cancel the effect of the disturbance force, the ideal structure of  $G_{FF}$  is given by (4-15). However, since the result is an improper system (*i.e.*, the numerator is of higher order than the denominator), the system is not physically realizable. As a simple alternative, the structure of (4-16) is proposed. The result is a simple first order lead compensator. Equation (4-16) is reasonable when the overall loop gain of  $F/V_{CMD} \gg 1$  and dominates the denominator of (4-16). Analytical results of the force feedforward controller were determined for the system in Figure 4-14 and are presented in Chapter V.

$$G_{FF} = -\frac{1}{\left\{ \frac{F}{V_{CMD}} \right\}} = -\frac{Ls + R + K_{CL}K_A}{K_{PA}K_AK_F} \quad (4-15)$$

$$G_{FF} = -\frac{1}{1 + \left\{ \frac{F}{V_{CMD}} \right\}} = -\frac{Ls + R + K_{CL} K_A}{Ls + R + K_{CL} K_A + K_{PA} K_A K_F} \quad (4-16)$$

An additional alternative to (4-16) is to invert the plant and then add “fast poles” to the resulting feedforward controller to make the system a proper one.

### LQG/LTR

Because of the arguments presented in Chapter II, the LQG/LTR strategy was chosen to determine an optimal and robust controller. Disturbance rejection characteristics of the position loop for the system can be shaped in the frequency domain using this technique.

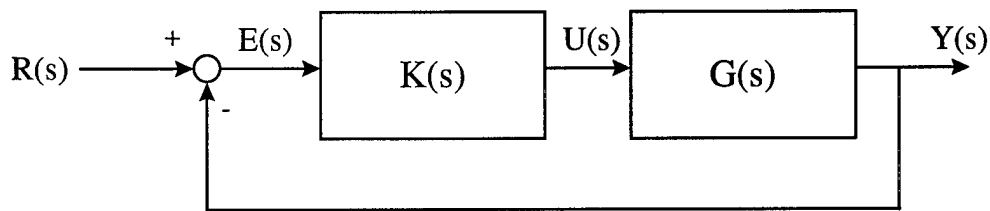


Figure 4-15. Controller/Plant Form of Block Diagram.

First, the system plant was isolated—that is—the amplifier, and the motor mechanical portion. The plant is given by:

$$\frac{y}{u} = \frac{K_{PA} K_A K_F}{Lms^3 + (bL + (R + K_{CL} K_A)m)s^2 + (b(R + K_{CL} K_A) + K_F K_B)s} \quad (4-17)$$

To facilitate the use of the multivariable LQG control, (4-17) was converted into state space form by multiplying the numerator and denominator by a “dummy” variable,  $Q(s)$ .

Defining:

$$x_1 = q(t) \Rightarrow \dot{x}_1(t) = x_2(t)$$

$$x_2 = \dot{q}(t) \Rightarrow \dot{x}_2(t) = x_3(t)$$

$$x_3 = \ddot{q}(t) \Rightarrow \dot{x}_3(t) = \frac{-(bL + m(R + K_{CL} K_A))}{Lm} x_3(t) - \frac{(b(R + K_{CL} K_A) + K_F K_B)}{Lm} x_2(t) + u(t)$$

$$y(t) = K_{PA} K_A K_F x_1(t)$$

Placing the above into matrix form:

$$\dot{\underline{x}}(t) = \begin{bmatrix} 0 & 1 & 0 \\ 0 & 0 & 1 \\ 0 & \frac{-(b(R + K_{CL} K_A) + K_F K_B)}{Lm} & \frac{-(bL + m(R + K_{CL} K_A))}{Lm} \end{bmatrix} \underline{x}(t) + \begin{bmatrix} 0 \\ 0 \\ \frac{1}{Lm} \end{bmatrix} u(t) \quad (4-18)$$

$$y(t) = [K_{PA} K_A K_F \quad 0 \quad 0] \underline{x}(t)$$

The next step of the design process is to design the target feedback loop (TFL). The target feedback loop should display the characteristics of the desired closed-loop transfer function. To choose the gain matrix for the TFL, a Kalman filter was designed

by varying the covariance matrices  $W_n$  and  $V_n$ . In the SISO case of the linear motor system, these matrices correspond to constant terms. Matlab code was developed to determine Kalman Filter gains and plot the sensitivity and closed-loop principal gains of the resulting target feedback loop.

To assess performance, in addition to closed-loop response, one can inspect the principal gains of the sensitivity and closed-loop or complementary sensitivity to predict performance with regard to tracking and disturbance rejection. There is a tradeoff between the bandwidth of the system response to inputs and low sensitivity to disturbance inputs. Sensitivity of the nominal system shown in Figure 4-15 to a disturbance at the output is given by

$$S(s) = \frac{1}{1 + G(s)K(s)} \quad (4-19)$$

and the closed-loop or complementary sensitivity is given by

$$T(s) = \frac{G(s)K(s)}{1 + G(s)K(s)} \quad (4-20)$$

It is easily demonstrated that

$$T(s) + S(s) = I \quad (4-21)$$

What (4-21) says is that even if sensitivity to disturbance,  $S(s)$ , approaches zero, the gain of closed-loop transfer function,  $T(s)$ , approaches unity and will have a sluggish response (33). This tradeoff is illustrated by manipulation of the linear motor system of Figure 4-16. To maximize dynamic stiffness, one aims to minimize the principal gain of the system sensitivity, while understanding that the tracking response will suffer.

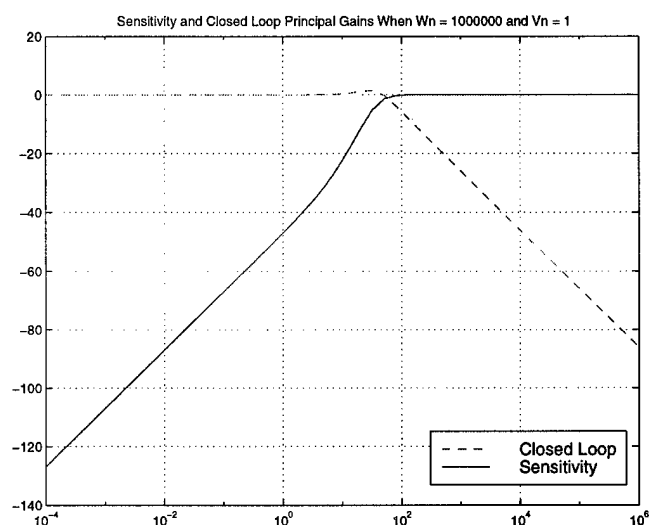


Figure 4-16. Sensitivity and Closed-Loop Principal Gains for One TFL.

Once the Kalman filter gains yield a desirable TFL, the next step is to design the LQG controller. The tradeoff here is accomplished by adjusting the control cost function,  $R$ . A low control cost function will result in a controller that nearly recovers the TFL, but demands high levels of control energy and may result in saturation or excessive heat generation.



### Placing Existing Controller Poles as Close as Possible to LQG/LTR Controller

In the attempt to use the LQG/LTR technique on the fixed U-500 controller structure, it is first necessary to manipulate the block diagram given in Figure 4-1 to be in the form of Figure 4-15. After this manipulation, the resulting  $K(s)$  has 5 zeros and 4 poles whereas the resulting LQG/LTR controller from above has 2 zeros and 3 poles. There is no known method of molding the existing controller to directly correlate to the optimal design directly, given that they are of different order. Consequently, this approach was abandoned for this research.

### Conversion to Discrete-Time System for Digital Control

Because the ultimate goal of this research is to provide a control system that is straightforward to implement, some analysis was performed in the discrete domain to develop a model for use in a digitally implemented open-architecture control.

The first task was to convert the model of servo system to discrete time. To facilitate doing so, one could first apply the zero order hold to the system:

$$\frac{y}{u} = \frac{K_{PA} K_A K_F}{LMs^3 + (bL + m(R + K_{CL} K_A))s^2 + (b(R + K_{CL} K_A) + K_F K_B)s} \left( \frac{1 - e^{sT}}{s} \right) \quad (4-22)$$

Recalling that  $(1 - e^{-st}) = (z-1)/z$  and moving the  $s$  from the zero order hold as part of  $G(s)$ , the resulting  $z$ -transform will be:

$$G(z) = \left( \frac{z-1}{z} \right) Z \left\{ \frac{K_{PA} K_A K_F}{L M s^4 + (bL + m(R + K_{CL} K_A)) s^3 + (b(R + K_{CL} K_A) + K_F K_B) s^2} \right\} \quad (4-23)$$

### Chapter Conclusion

This chapter has provided a synopsis of the procedures used to identify and control the linear motor system's dynamic compliance. The experimental results of the fixed-structure controller as well as theoretical results of the alternative control approaches are presented in the following chapter.

## CHAPTER V

### RESULTS FOR DYNAMIC STIFFNESS MODULATION

Many of the results of this research are contained in Chapter IV as system identification was one of the major steps in the process. The following results show that the general shapes of the linear motor dynamic stiffness (as shown by its inverse—dynamic compliance) can be shifted toward objective shapes by adjusting controller gains. The results also demonstrate that the model predicts the dynamic compliance profiles reasonably well as various parameters are changed.

In addition to the experimental results using the Aerotech controller gains, analytical results are presented for the force feedforward and LQG/LTR controllers proposed in Chapter IV to motivate future implementation.

#### Changing Control Gains of Fixed Controller

Figure 5-1 shows the dynamic compliance of the system when the recommended factory-tuned gains as provided by the manufacturer are implemented. Agreement between model and experimental data is excellent in terms of the location and magnitude of the resonant peak. Low frequency agreement falters, but is attributed to poor coherence of the shaker data taken (below 0.5 below 50 rad/sec).

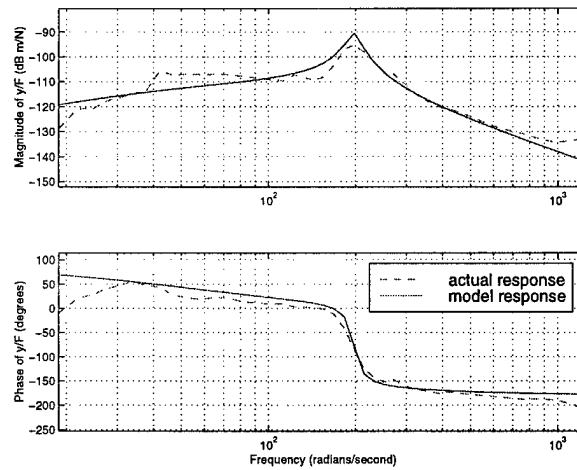


Figure 5-1. Dynamic Compliance of Linear Drive with Factory “Tuned” Gains.

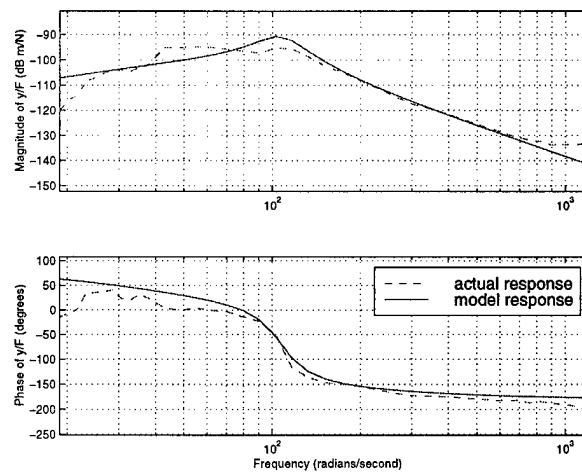


Figure 5-2. Gain Adjustment to Reduce Resonant Peak of Factory Gains.

The goal of the first adjustment was to limit the peak of Figure 5-1. Reduction of the position loop gain,  $K_{POS}$  served to increase damping by moving the complex poles closer to the real axis. The resulting compliance profile is shown in Figure 5-2.

### Shifting Resonant Frequency and Damping Ratio

Next, specific objectives for varying the damping ratio and shifting the resonant frequency to target locations are undertaken. Figure 5-3 shows the resulting dynamic compliance when a damping ratio of 0.05 was sought. As would be expected, a large resonant peak is present and coincides reasonably well with the profile predicted by the model. Figure 5-4 shows the profile obtained when a damping ratio of 0.95 is sought. The result correlates well to a high damping ratio as there is no visible peak in the profile and the response appears smooth across the frequency range.

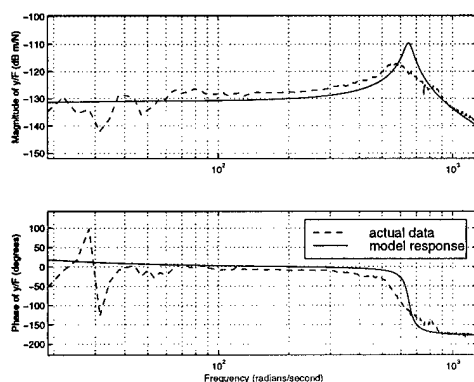


Figure 5-3. Experimental and Model Response for  $\xi=0.05$ .

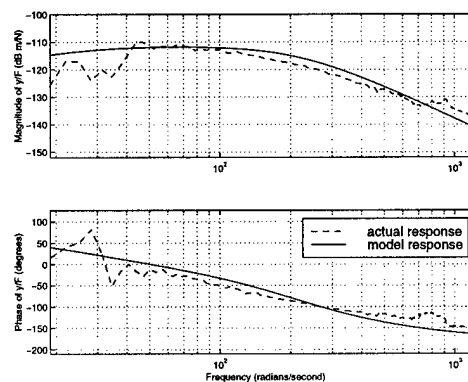


Figure 5-4. Experimental and Model Response for  $\xi=0.95$ .

Figure 5-5 through Figure 5-10 are the compliance profiles resulting from the gains computed to target specific resonant frequencies. Figure 5-5 shows the most

obvious mismatch between the response predicted by the model and that obtained experimentally.

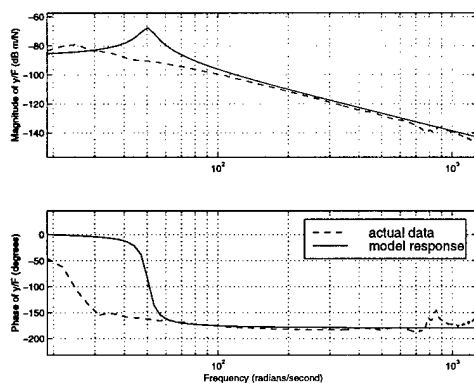


Figure 5-5. Target  $\omega_n=50$  rad/s.

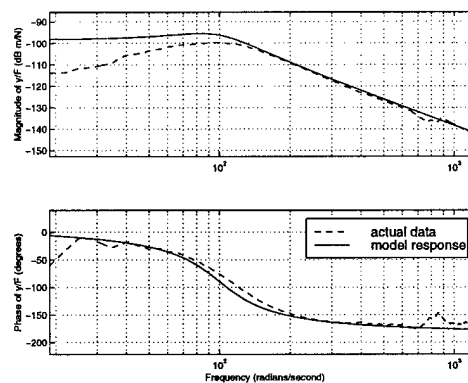


Figure 5-6. Target  $\omega_n=100$  rad/s.

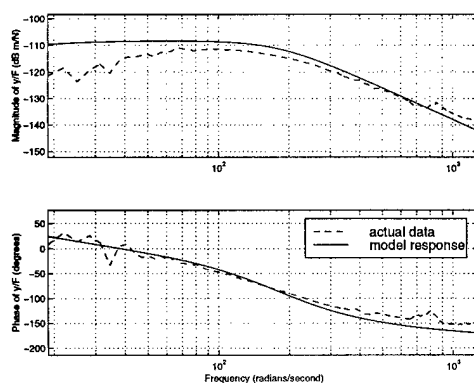


Figure 5-7. Target  $\omega_n=200$  rad/s.

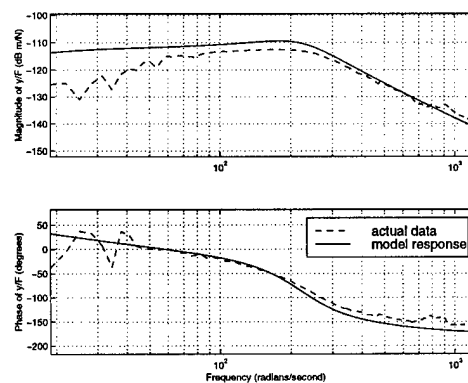
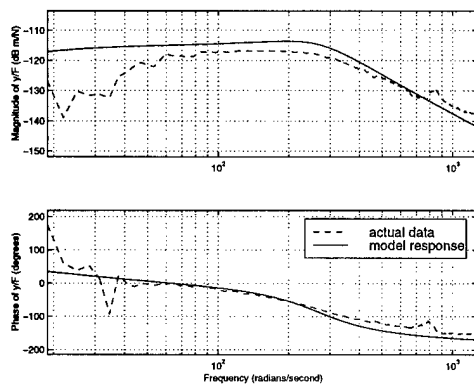
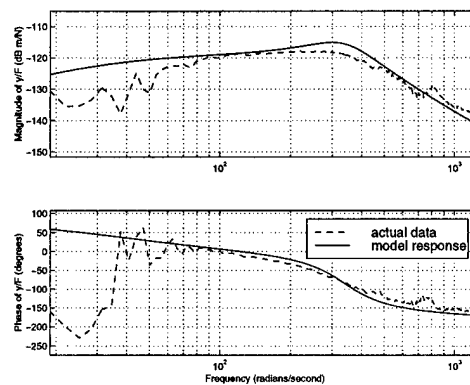


Figure 5-8. Target  $\omega_n=250$  rad/s.

Figure 5-9. Target  $\omega_n=300$  rad/s.Figure 5-10. Target  $\omega_n=400$  rad/s.

The control gains used in obtaining Figure 5-5 through Figure 5-10 are given in Table 5-1. The trend illustrated is that to obtain higher resonant frequencies based on the second-order assumption of the dominant complex poles, overall loop gain must be higher.

Table 5-1. Control Gains Used for Target Resonant Frequencies.

Target $\omega_n$ (rad/sec)	50	100	200	250	300	400
$K_{POS}$	1	1	120	240	250	400
$K_I$	1300	5000	1600	1400	2100	4700
$K_P$	0	150000	520000	400000	550000	550000

### Analytical Results for LQG/LTR

To demonstrate how the LQG/LTR method can analytically change the dynamic compliance, analytical results are obtained using this technique. The following simulation results are presented to show the general effect of changing design parameters,  $W$ ,  $V$  and  $R$ . Principle gains of the closed-loop sensitivity and complementary closed-loop sensitivities are plotted beside each analytical dynamic compliance response to illustrate the impact of the adjustments on the tradeoff between disturbance rejection and closed-loop performance.

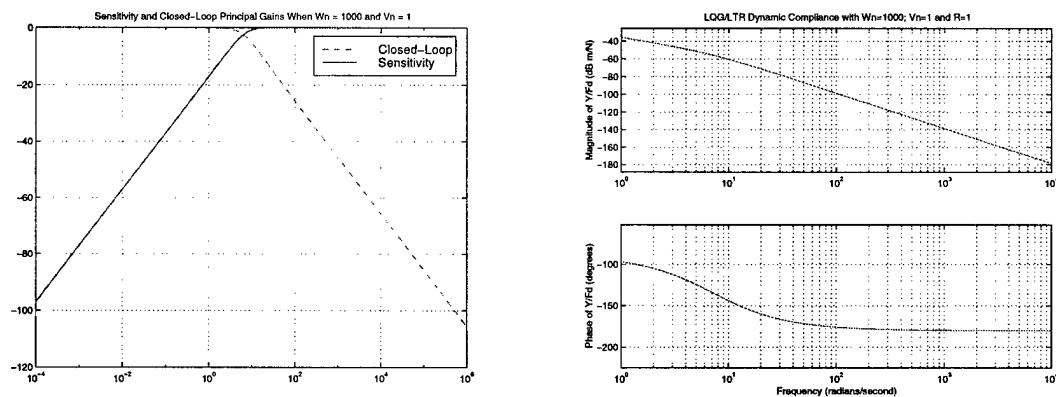


Figure 5-11. LQG/LTR Results with  $W_n=1000$ ,  $V_n=1$  and  $R=1$ .



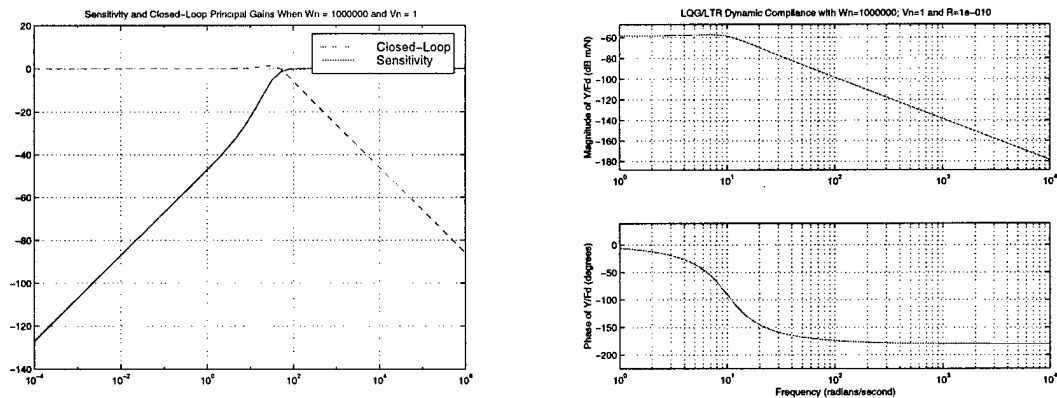


Figure 5-12. LQG/LTR Results with  $W_n=10^6$ ,  $V_n=1$  and  $R=10^{-10}$ .

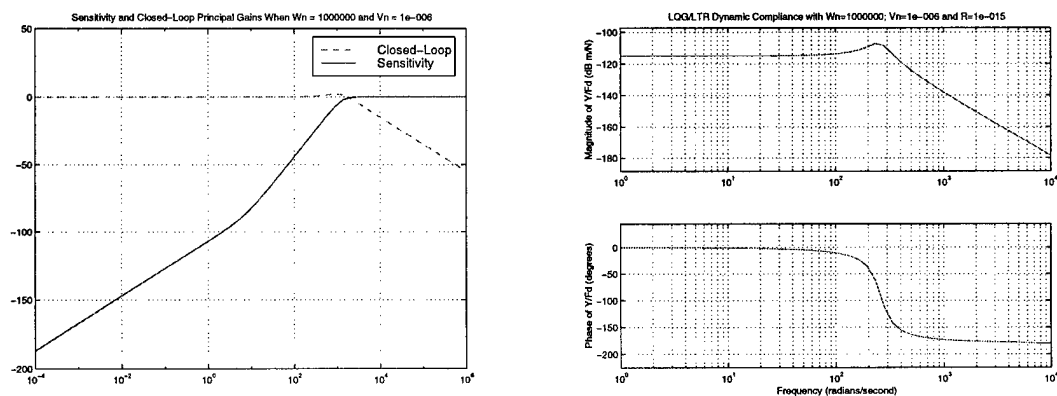


Figure 5-13. LQG/LTR Results with  $W_n=10^6$ ,  $V_n=10^{-6}$  and  $R=10^{-15}$ .

Before attempting to implement the control illustrated above, one must temper the objectives with the constraints posed by the limits of control energy and gain. For example, in Figure 5-13, tremendous control energy is required because the cost of

control,  $R$ , was given a very low value. Consequently, the resulting closed-loop system results in complex poles in the neighborhood of  $s = -3000 \pm 4500j$ . The highest gains used on the fixed Aerotech controller moved the pair of complex poles to only  $s \approx -125 \pm 225j$ . One can, therefore, deduce that the profile shown by Figure 5-13 would require very large inputs and is, therefore, probably not physically realizable.

#### Force Feedforward Control

Analytically, the first order feedforward controller proposed in Chapter IV decreased dynamic compliance (increased dynamic stiffness) by approximately 25 dB for every frequency in the experimental range. Despite the attenuation of the dynamic compliance magnitude, the controller had little effect on the dynamics (*i.e.*, the shape) of the compliance.

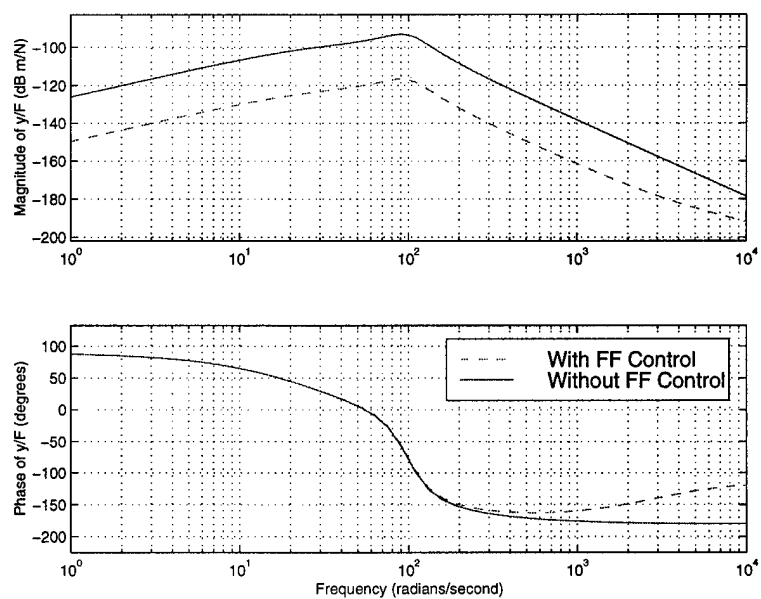


Figure 5-14. Dynamic Compliance--Force Feedforward Compensation.

## CHAPTER VI

### DISCUSSION/CONCLUSIONS

#### Challenges for Modulating Dynamic Stiffness

The shaping of dynamic compliance (and therefore dynamic stiffness) presents a unique problem from most topics addressed in existing control literature. Most research conducted in the area of "loop shaping" deals with the response to a direct control input to the system and addresses only the system's ability to minimize the disturbance response. The response to the disturbance can, therefore, not be controlled in a direct sense since we cannot alter the input itself. Control is applied through feedback to reduce the *effect* of the disturbance on the plant.

#### Assessment of Model Performance

The experimental results of Chapter V demonstrate that the shape of dynamic compliance response can be altered and that the model generally predicts the shape. There are several factors which affect model performance. The model is least accurate at low frequencies. First, since the force sensor on the shaker is a piezoelectric element designed for dynamic force measurement, low frequency force measurement data is generally less accurate. Also, the force applied by the shaker is proportional to excitation frequency squared. As a result, the magnitude of the force applied to the stage at low

frequencies is much smaller than at higher frequencies and may not provide ample excitation of the system for measurement. Another factor at low frequencies is the possibility of stiction on the linear bearing track because the force level may not be high enough to completely overcome static friction with each change of direction.

Besides low frequency mismatch, the model displayed decreased performance at lower controller gains like those used to generate Figure 5-5. The lower gains applied to the system tend to move the complex poles closer to the real axis. As these poles approach the real axis, the parameter sensitivity approaches infinity and any model inaccuracies are amplified (36).

#### Predicting Damping Ratios and Resonant Frequencies

The algorithm used to select control gains to meet target damping ratios and natural frequencies, as described in Chapter IV, is based on a second order approximation and assumes that the complex poles of the compliance dominate the response. At certain gain values, the approach used to predict the location of the resonant frequency deviates from both the 4<sup>th</sup> order model and the experimental results because the complex poles move farther away from the imaginary axis and the pole on the real axis dominates the transient response. By comparing the gains in Table 4-2 with those in Table 5-1, one can predict whether or not the second-order approximation is valid.

### Limitations of Fixed-Structure Controller

A limiting factor of this research was the use of the Aerotech control structure. The scaling and fixed PI structure of only the velocity loop limited the ability to shape dynamic compliance. Figure 6-1 through Figure 6-3 show the limited effect control gains have on the dynamic compliance profile. The plots show the gain of dynamic compliance varying one control parameter at a time, while holding others at a nominal value.

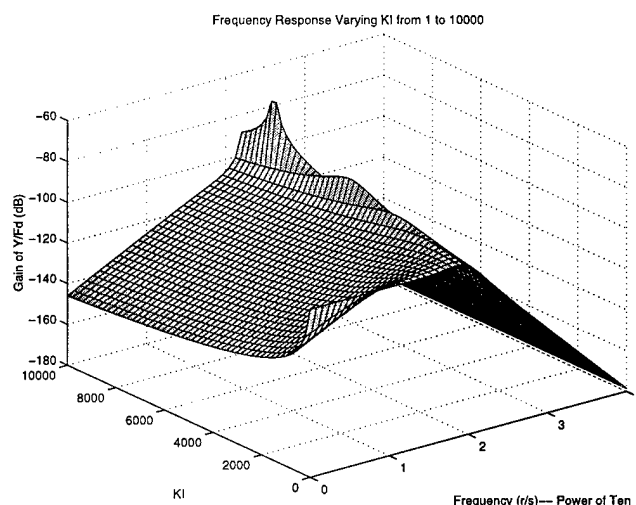


Figure 6-1. Dynamic Compliance Across Range of  $K_I$ .

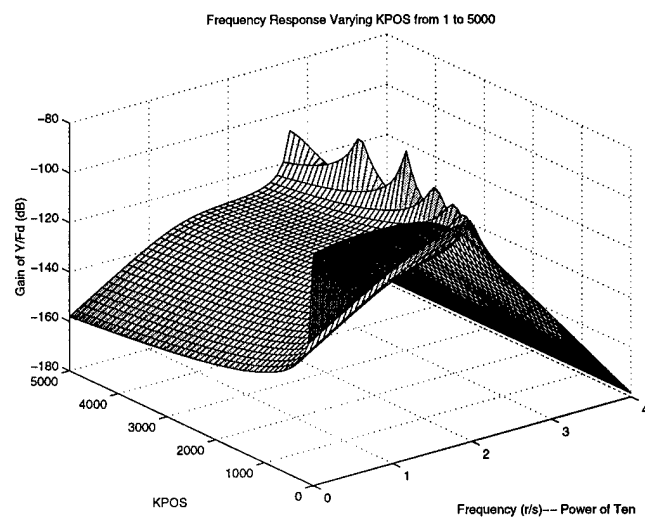


Figure 6-2. Dynamic Compliance Across Range of K<sub>POS</sub>.

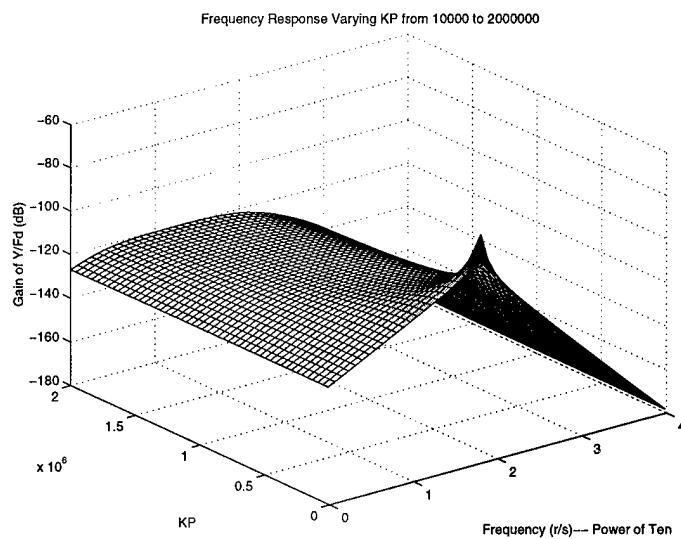


Figure 6-3. Dynamic Compliance Across Range of K<sub>P</sub>.

### Assessing the Usefulness of Alternate Control Approaches

Although LQG/LTR is a valuable control tool, its main objective is to shape the response of a control input. As such, the main drawback to the use of the LQG/LTR approach is that, in its goal to shape command following and disturbance rejection, there is no immediate correlation of a TFL to dynamic compliance. Instead, compliance must be backed out as a consequence of the command-following objective function. If the goal is to directly shape the disturbance transfer function, one must first design for the level of open-loop disturbance sensitivity. After determining an acceptable level of sensitivity, the next step is to design the controller. The last step is then to back out the disturbance response. This process is far from a direct approach for compliance control. One could look at the problem as a regulation problem (*i.e.*, no commanded input) and manipulate the block diagram of the system to fit the structure of Figure 4-15 where  $F_d$  is the input. Before proceeding on this approach, however, it is vital to review the overall problem. The disturbance in this context is not a signal—it is a force and acts on the mechanical portion of the system. As such, one cannot disconnect the disturbance from the mechanical section of the plant, even though it seems possible in a mathematical context through block diagram algebra. Some investigation could be conducted to determine the applicability of LQG/LTR or similar technique in the design of a force feedforward controller to obtain a desired response.

The feedforward controller has the potential for increasing the stiffness, but one must look at the possibility of saturating the amplifier in a particular application. The



non-linear saturation could reduce the system stability. Also, as analytical results indicated, the design presented had no effect on the shape of the response—only its scaling. As mentioned above, some investigation should be conducted into the feasibility of frequency response shaping by the use of a more sophisticated feedforward controller.

### Conclusion

Machining research has established that dynamic stiffness is the primary factor in determining the quality of a machine tool's finished parts, and the stability and efficiency of the machining process.

Recent advances have made brushless linear motors the subject of close inspection and assessment by the machine tool industry for use as main feed mechanisms. Inherent benefits of brushless linear DC motors include extremely accurate positioning, high velocity and acceleration as well as the elimination of nonlinearities such as backlash and hysteresis. Fewer moving parts also mean less maintenance and fewer components to fail. Although these benefits have prompted several manufacturers to employ linear motors as main feed mechanisms in some machine tools, the ability to shape the dynamic stiffness profile of the machine tool is one important benefit that has largely been unexplored.

This research has shown that dynamic stiffness of the linear drive system can, in fact, be modeled reasonably accurately and can be altered by changing nothing more than controller parameters. Such reshaping of the dynamic stiffness for a traditional machine

tool feed mechanism would not be possible except by the complete restructuring of its mechanical components.

The experimental results of this research shown in Chapter V demonstrate the ability to alter dynamic compliance (and therefore dynamic stiffness) to meet approximate target shapes. Resonant peaks can be moved to different frequencies, reduced or eliminated by changing control gains.

The use of the fixed-structure controller limits the ability to shape the response. The analytical results of the feedforward controller and LQG/LTR controller show that other structures may have more success in shaping the response to fit desired profiles.

## CHAPTER VII

### RECOMMENDATIONS FOR FUTURE WORK

In pursuing the overall goal of optimizing dynamic stiffness for a machining process, the following recommendations are provided.

#### Use a Linear Motor in a Machining Process to Assess Its Relative Merits

To connect the results obtained in this research to the machining process, a linear drive should be employed to perform a simple machining operation as in (1). By performing analysis on the actual machining process, results could be compared to those obtained from conventional feed mechanisms to assess any benefits derived from dynamic stiffness shaping. Some consideration should be given to the use of a drive system with higher current capacity to allow realistic levels of cutting or grinding forces without saturation of amplifier and motor dynamics. The linear drive used in this research can deliver a constant force of only 53 Newtons (12 lbs.).

#### Open-Architecture Controller

To obtain experimental results for variable control configurations without extensive hardware or circuitry changes, an open-architecture state space controller should be developed to digitally implement a given control structure. Such a controller would allow experimentation using a variety of control approaches and subsequent

determination of the best structure for the shaping of dynamic stiffness. This controller would also facilitate the goal of experimentation on tracking control as discussed below.

#### Develop Tracking Control Concurrently to Optimize Tradeoff with Compliance Control

This research has focused exclusively on dynamic stiffness. No consideration was given to the resulting control's effect on position tracking. A method for characterizing and optimizing the tradeoff between tracking control and dynamic compliance shaping for a given machining process should be developed.

#### Model Brushless Motor Phases

As mentioned in Chapter IV, simplifications were made in the development of the brushless motor model. Future work should incorporate the non-linear effect of three-phase current commutation. The dependence of current developed in the motor coil on phase angle provides a challenge in developing a traditional model. One possible suggestion is the use of Simulink to model the nonlinearities presented from phase dependence, magnetic flux saturation and cross-inductance of the three coils.

## REFERENCES

- (1) Alter, David M. Control of Linear Motors for Machine Tool Feed Drives. Doctoral Thesis, University of Illinois, Urbana-Champaign, 1994.
- (2) Handbook for Brushless Motors and Drive Systems. Kollmorgen Inland Motor, Radford, Va.
- (3) Slemon, Gordon R. Electric Machines and Drives. Reading: Addison Welsley Publishing Company, Inc., 1992.
- (4) Pillay, Pragasan and Krishnan, R. *Modeling of Permanent Magnet Motor Drives*. IEE Transactions on Industrial Electronics, vol. 35, No. 4, pp 537-541, November, 1988.
- (5) Basak, Amitava. Permanent Magnet DC Linear Motors. Oxford: Clarendon Press, Inc., 1996.
- (6) Eidelberg, Boaz. *The Linear Motor Option*. Power Transmission Design., April, 1996, pp. 37-40.
- (7) Beradinis, Lawrence A., and Gyorki, John R.. *Electric Drives: Gearing Up for Instant Automation*. Machine Design, April 18, 1994, pp. 46-51.
- (8) Aronson, Robert B. *Attack of the Linear Motors*. Manufacturing Engineering, May 1997, pp. 60-71.
- (9) Aronson, Robert B. *Machine Tool 102: Way Design*. Manufacturing Engineering, January 1995, pp. 41-47.
- (10) Valenti, Michael. *Machine Tools Get Smarter*. Mechanical Engineering, November 1995, pp 71-75.

- (11) Serway, Raymond A. Physics for Scientists and Engineers. Philadelphia: Saunders College Publishing, 1986.
- (12) Rivin, Eugene I. and Kang, Hongling. *Improvements of Machining Conditions for Slender Parts by Tuned Dynamic Stiffness of Tool*. International Journal of Machine Tools Manufacturing. Vol. 29, No. 3. pp. 361-376, 1989.
- (13) Kelson, Z.Y. Yen and Hsueh, Wen C. *Suppression of Chatter Vibration Inner-Diameter Cutting*. JSME International Journal, Series C, Vol. 39, no. 1, pp. 25-33. 1996.
- (14) Esayed, M.A., et al. *Evaluation of Process Damping and its Effect on Stability in Turning*. Engineering Systems Design and Analysis Conference, Vol. 9, pp. 83-92. 1996
- (15) Alter, D.M. and Tsao, Tsu-Chin. *Stability of Turning Processes with Actively Controlled Linear Motor Feed Drives*. Transactions of the ASME, Vol. 116, pp.298-307, August, 1994.
- (16) Xu, Ming and Birchmeier, John R. *Dynamic Stiffness Testing and Its Applications in Machine Tools*. Sound and Vibration, pp. 14-23. June 1997.
- (17) Jenkins, Hodge E. and Kurfess, Thomas R. *Dynamic Stiffness Implications for a Multi-Axis Grinding System*. Journal of Vibration and Control, vol. 3, no. 3, pp. 297-313. Thousand Oaks CA: Sage Sci Press USA, Aug 1997.
- (18) Elbestawi, M.A. and Sagherian, R. *Dynamic Modeling for the Prediction of Surface Errors in the Milling of Thin-Walled Sections*. Journal of Materials Processing Technology. Vol. 25, (1991) pp. 215-228.
- (19) Lee, Hwa Soo and Furukawa, Yuji. *On the Method to Determine Dynamic Stiffness of Grinding Machines*. Bulletin of the Japanese Society of Precision Engineering. Vol. 22, No. 2, June 1988.

- (20) Franklin, G.F., Powell, J.D. and Workman, M.L. Digital Control of Dynamic Systems. Reading, MA: Addison-Wesley Publishing Company, 1994.
- (21) Matlab Signal Processing Toolbox User's Guide. Natick, MA: The Mathworks, Inc., 1996.
- (22) Tung, Ka-Lun, and Yam, Yeung. *System Identification and Control Synthesis for a Benchmark Problem*. IEEE Transactions on Control Systems Technology, vol. 6, No. 1, pp. 103-110, January, 1988.
- (23) Egami, Tadashi and OkaBayashi. *Disturbance Supression Control With Preview Action for a Linear DC Brushless Motor*. Electrical Engineering in Japan, Vol 113, No. 6, 1993, pp. 122-130.
- (24) Phillips, Charles L. and Harbor, Royce D. Feedback Control Systems. Englewood Cliffs, NJ: Prentice-Hall, 1988.
- (25) Ogata, Katsuhiko. Modern Control Engineering. Englewood Cliffs, NJ: Prentice Hall, 1990.
- (26) Ohishi, Kiyoshi. *Robust Control of a DC Servomotor Based On Linear Adaptive Control System*. Electrical Engineering in Japan, Vol. 108D, No. 1, January, 1988, pp. 39-45.
- (27) Athans, Michael . *A Tutorial on the LQG/LTR Method*. Proceedings of the American Control Conference., pp. 1289-1296. New York: IEEE, 1986.
- (28) Phillips, Charles L., and Nagle, H. Troy. Digital Control System Analysis and Design. Englewood Cliffs, NJ: Prentice-Hall, Inc., 1990.

- (29) Byrns, Edward V., Jr, and Calise, Anthony J. *Further Development of an Approximate Loop Transfer Recovery Methodology for Fixed Order Dynamic Compensator Design*. Optimal Control Applications and Methods, Vol. 15, pp. 123-132, 1994.
- (30) Shafai, B, Keel, L.H., and Beale, S.. *Zero Assignment and Loop Transfer Recovery in the LQG design*. Proceedings of the 29<sup>th</sup> Conference on Decision and Control , vol. 3, pp. 1217-1221. Piscataway, NJ: IEEE, 1990.
- (31) Bainum, P.M. and Tan, Z.. *The Digital LQG/LTR Controller with a Compensated Observer for a Tethered Reflector/Antenna System*. Acta Astronautica, vol. 38, pp. 15-23. Great Britain: Elsevier Science, Ltd, 1996.
- (32) Grimble, M.J.  *$H_\infty$  Controllers with a PID Structure*. Journal of Dynamic Systems, Measurement and Control, Vol. 112, pp. 325-336, September, 1990.
- (33) Maciejewski, J.M. Multivariable Feedback Design. Wokingham, UK: Addison-Wesley Publishers, Ltd., 1994.
- (34) Alter, David M. and Tsao, Tsu-Chin. *Dynamic Stiffness Enhancement of Direct Linear Motor Feed Drives for Machining*. Proceedings from the American Control Conference, pp. 3303-3307. June 1994.
- (35) Gere, James M, and Timoshenko, Stephen P. Mechanics of Materials. Boston: Kent Publishing Company, 1984.
- (36) Kurfess, T.R., and Nagurka, M.L. *A Geometric Representation of Root Sensitivity*. Journal of Dynamic Systems, Measurement and Control, Vol. 116, pp. 305-309, June, 1994.